Large-scale Comparison of Fe and Ru Polyolefin C-

H Activation Catalysts

Husain Adamji¹, Ilia Kevlishvili¹, Aditya Nandy^{1,2}, Yuriy Román-Leshkov^{1,2}, and Heather J. Kulik^{1,2,*}

¹Department of Chemical Engineering, Massachusetts Institute of Technology, Cambridge, MA 02139, USA

²Department of Chemistry, Massachusetts Institute of Technology, Cambridge, MA 02139, USA

*Corresponding author email: hjkulik@mit.edu

ABSTRACT: We performed a large-scale density functional theory comparison of polyolefin C—H hydroxylation trends across over 200 Fe and Ru catalysts that are identical except for their metal centers for the radical-rebound conversion of propane to propanol. We observed a strong spin-state dependence: higher-spin states had more favorable metal-oxo formation and isopropanol release in Ru catalysts, while hydrogen atom transfer (HAT) was more favorable in Fe catalysts. While the widely studied metal-oxo formation vs. HAT linear free-energy relationship held for Ru, it was more easily disrupted for Fe. Ru catalysts have a spin-forbidden C—H hydroxylation pathway, while Fe catalysts favor a spin-allowed, intermediate spin pathway. Calculation of reaction coordinates on representative catalysts corroborated these spin—reactivity trends and showed comparable energetic spans for Fe and Ru analogues, as well as strong Brønsted—Evans—Polanyi relationships for both the metal-oxo formation and HAT steps, motivating expanded study of Fe catalysts.

Keywords: polyolefin C–H activation; radical rebound; iron; ruthenium; density functional theory; high-throughput screening; spin-state-dependent catalysis

1. Introduction.

Polyolefins are high-volume, low-cost thermoplastics with high tensile strength, ductility, thermal stability, and chemical inertness. ^{1,2} The high demand for polyolefins is driven by their durability and versatility with annual production scales greater than 150 million tons, constituting 40% of global plastic production.³ While their primary application is in the packaging industry, polyolefins have also found utility in electrical insulation, pipes, automotive components, and medical devices.^{3,4} However, their mechanical resilience and chemical inertness constrain their potential applications due to their inability to be interfaced with polar additives or fillers.⁵ Additionally, the challenge of recycling polyolefins is evident, with only 14% of polyethylene recycled as recently as 2015.⁶ These low recycling rates are a consequence of destructive chain scission events during mechanical reprocessing or chemical modification recycling approaches that degrade their thermomechanical properties.^{7,8} Ongoing efforts have, thus, focused on the incorporation of polar groups into polyolefins to enhance their properties, aiming to create higher-value polymers with a broader range of applications and improved recyclability.^{2,4,9,10}

Several approaches have been developed for the introduction of polar functional groups into polyolefins. Copolymerization of an α -olefin with a polar monomer is one approach that has been studied extensively, $^{2,5,10-14}$ yet demonstration of this approach has been limited because the transition metal catalysts used in copolymerization are either poisoned by polar comonomers or exhibit insufficient catalytic activity in their presence. $^{10,15-17}$ A more promising approach involves the functionalization of C–H bonds in polyolefins. 2,18,19 While free radical-mediated processes 20 can be used here, they often lack chemoselectivity, leading to undesirable β -scission or crosslinking side reactions that compromise improvements in the physical properties of polyolefins. 23,24 Transition-metal catalyzed C–H functionalization in polyolefins, exemplified by

Rh,²⁵⁻²⁷ Cu,²⁸ Ir,²⁹ Mn,³⁰ and Ni³¹ catalysts has succeeded in minimizing deleterious side reactions, yet many of these catalysts exhibit low turnover numbers. To gain a deeper understanding of transition metal-catalyzed C–H functionalization in polyolefins, first-principles calculations are invaluable for identifying promising active site motifs and deciphering reaction mechanisms and their corresponding energy profiles. Notably, C–H oxidation in polyolefins involves a highly active but transient metal-oxo intermediate³⁰⁻³³ for C–H activation³⁴ akin to those observed in enzymes,³⁵⁻³⁷ and other homogeneous³⁸⁻⁴² and heterogeneous catalysts.⁴³⁻⁴⁸ Computation can elucidate the role of this fleeting metal-oxo species, which is difficult to characterize experimentally.⁴⁹⁻⁵⁴ It can also aid in unraveling the influence of spin state on reactivity⁵⁵⁻⁵⁸ and the manifestation of multistate reactivity,⁵⁸⁻⁶² both crucial for optimizing catalytic activity in C–H oxidation.

A recent experimental study reported the catalytic oxidation of C–H bonds in polyethylene using a homogeneous polyfluorinated Ru porphyrin catalyst that can selectively incorporate carbonyl and hydroxyl functional groups with high turnover numbers.³² On the contrary, Fe catalysts with proven activity for the oxidation of aliphatic *sp*³ C–H bonds, such as Fe porphyrin,⁶³ the White-Chen catalyst (Fe(PDP)),⁶⁴ and an Fe complex comprising the oxidatively robust tetradentate BpyPY₂Me ligand,⁶⁵ did not demonstrate substantial activity for polyethylene oxidation, which was attributed to the incompatibility of the Fe catalysts with the reagents and reaction conditions.³² However, this study evaluated only three Fe catalysts due to the practical constraints associated with extensive experimental screening. Thus, it could not definitively confirm the inactivity of Fe catalysts relative to Ru catalysts for C–H oxidation of polyolefins. Given the ubiquity of C–H activation catalysts containing the relatively earth-abundant Fe as the metal center,⁶⁶⁻⁷⁰ calculations are well suited to facilitate screening over larger numbers of Fe and

Ru catalysts and could provide a more comprehensive comparison of their polyolefin oxidation activities. Indeed, high-throughput screening, guided by density functional theory (DFT) calculations, has facilitated the evaluation of catalyst activity for C–H activation across diverse, large design spaces.⁷¹⁻⁷⁶

The computational cost of DFT-based screening is often lowered by scaling relations, such as Brønsted–Evans–Polanyi (BEP) relationships between activation and reaction energies ⁷⁷⁻⁷⁹ and linear free-energy relationships (LFERs) between distinct thermodynamic steps, ⁸⁰⁻⁸² that draw linear correlations between DFT-computed descriptors and reaction parameters. ^{75,83-90} For example, ligand field strength has been shown to correlate with C–H activation reactivity of Fe catalysts. ^{72,86,91,92} These scaling relations, however, are readily disrupted by varying metal identities, oxidation, and spin states in open-shell transition metal catalysts. ^{71,72,74} Additionally, scaling relations have also been shown to be altered or broken by changes to metal-local structure ^{79,91,93} or non-covalent interactions ^{91,94,95} that can influence the stability of certain reaction intermediates over others. When searching over a large set of Fe and Ru catalysts to identify promising candidates for polyolefin C–H oxidation, it is important to examine the applicability of scaling relations to ascertain whether manipulation of ligand field strength is a valid strategy to tune C–H activation reactivity in Ru catalysts.

In this work, we perform high-throughput computational screening to compare trends in C–H hydroxylation reactivity of an initial catalyst set containing over 1500 mononuclear, homogeneous Fe and Ru catalysts at a single +2 oxidation state and three spin states. We curate a subset of over 200 catalysts that are identical except for their metal center (i.e., Fe vs Ru) to isolate metal dependence. We demonstrate that differences in C–H activation energetics between Fe and Ru catalysts are sensitive to the spin state. We also show that widely employed LFERs in C–H

activation do not generalize for both Fe and Ru or across spin states, yet Fe catalysts present a greater opportunity to disrupt LFERs compared to Ru catalysts when evaluated over all spin states. We propose C–H hydroxylation spin–reactivity trends for both metals as deduced from spin splitting energies. Finally, we compute full free energy landscapes for representative Fe and Ru catalysts to compare their kinetics and catalytic turnover frequencies and examine the validity of BEPs in C–H activation catalysis for polyolefin functionalization.

2. Reaction Mechanism and Catalyst Datasets.

We evaluate trends in our Fe and Ru catalysts by studying their activity for polyolefin functionalization via C-H hydroxylation. We assume that C-H activation in polyolefins occurs via the widely-recognized radical rebound mechanism. 96 To balance computational cost and realism in our high-throughput DFT-based studies on transition metal catalysts, we first performed control DFT calculations to identify a suitable model compound for long-chain polymers using a representative catalyst (Supporting Information Figure S1 and Text S1). Here, we investigated the influence of alkane chain length and metal-local steric interactions stemming from hydrocarbon branching on the radical rebound reaction energetics. We find that both long-range interactions arising from carbon atoms that are distant from the metal active site as well as steric interactions from nearby branched substituents have negligible influence on the reaction energetics (Supporting Information Figure S1 and Text S1). Thus, we select propane as our model compound for polyolefins that undergo C-H activation at a secondary carbon, which in this case forms isopropanol. We calculate the reaction energetics for the radical rebound propane-to-isopropanol conversion over mononuclear Fe and Ru complexes in a single oxidation state (i.e., M(II)), excluding higher oxidation M(III) catalysts since they seldom have as favorable radical rebound energetics as M(II) catalysts.⁷² In the radical rebound mechanism catalytic cycle, the open metal

site in the square pyramidal resting state structure (**R**) of the catalyst undergoes two-electron oxidation to form a high-valent terminal metal-oxo species (=**O**), which we model using the common oxidant N₂O as the oxygen atom source (Figure 1). The reaction energy (see Sec. 3) for the metal-oxo formation, ΔE (oxo) is computed as:

$$\Delta E(\text{oxo}) = E(=0) + E(N_2) - E(R) - E(N_2O)$$

Alternative oxidants (e.g., O_2 or H_2O_2 or 2,6-dichloropyridine 1-oxide, which was used in previous experimental studies³²) would rigidly shift the reaction energetics without affecting relative energetics (Supporting Information Table S1). The terminal M(IV)=O species is highly reactive and catalyzes a hydrogen atom transfer (HAT) step in which a hydrogen atom from the secondary carbon of propane is abstracted to form a metal-hydroxo intermediate (**-OH**) (i.e., M(III)-OH) and an isopropyl radical (Figure 1). The reaction energy for this step, $\Delta E(\text{HAT})$, is given by:

$$\Delta E(HAT) = E(-\mathbf{OH}) + E(\bullet CH(CH_3)_2) - E(=\mathbf{O}) - E(C_3H_8)$$

The isopropyl radical recombines with the M(III)–OH moiety (**-OH**) in the radical rebound step to form the isopropanol-bound intermediate (**-IPA**). The active site is then regenerated following the release of isopropanol to recover the resting state structure (**R**) (Figure 1). The isopropanol release energy, ΔE (release) is calculated as:

$$\Delta E(\text{release}) = E(\mathbf{R}) + E((\text{CH}_3)_2\text{CHOH}) - E(-\mathbf{IPA})$$

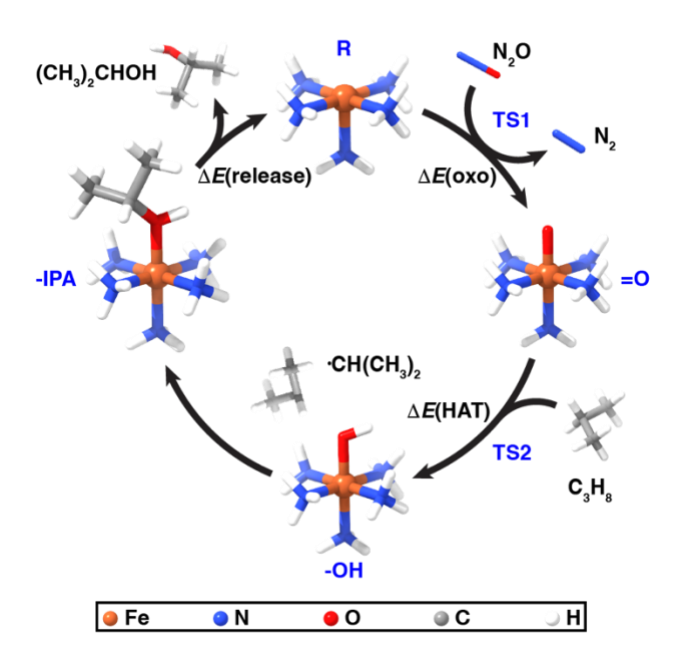


Figure 1. Catalytic cycle for the radical rebound hydroxylation of propane to isopropanol at the Fe active site of a representative square pyramidal homoleptic complex with identical ammonia ligands. Starting with the resting state (**R**) in the oxidation state of II, the cycle progresses clockwise to first form the metal-oxo species (**=O**) from N₂O, the metal-hydroxo species (**-OH**) through HAT from propane at the secondary carbon, and the isopropanol-bound species (**-IPA**) following isopropyl radical rebound. Color codes: Fe in brown, N in blue, O in red, C in gray, and H in white.

All resting state and isopropanol-bound d^6 intermediates of the Fe and Ru catalysts were studied in three spin states: low spin (LS) i.e., S = 0 (singlet), intermediate spin (IS) i.e., S = 1 (triplet), and high spin (HS) i.e., S = 2 (quintet) (Supporting Information Table S2). The metal-oxo intermediates for d^4 Fe(IV)=O and Ru(IV)=O adopt an identical spin state as their corresponding d^6 resting states. During HAT, for Fe catalysts, we assumed a ferromagnetically coupled H• (α -radical transfer) with an antiferromagnetically coupled •CH(CH₃)₂ that recombines with the metal-hydroxo species during the rebound step, as done in prior work. For Ru catalysts, however, we assumed an antiferromagnetically coupled H• (β -radical transfer) with a ferromagnetically coupled •CH(CH₃)₂ recombining with the metal-hydroxo species because higher spin multiplicity Ru-hydroxo species are highly unfavorable, as observed from differences in spin state energies (see

Sec. 4b). Thus, the overall spin state is conserved in the metal-hydroxo intermediate when coupled with the isopropyl radical as well as in the isopropanol-bound intermediate and ultimately, throughout the catalytic cycle.

In this work, our data set of mononuclear square pyramidal Fe and Ru catalysts consists of complexes both with monodentate ligands only and complexes with macrocyclic ligands. The complexes with monodentate ligands were inspired by prior work⁹⁷ and comprise 70 homoleptic and heteroleptic structures in each spin state (i.e., LS, IS, and HS), resulting in 210 complexes for both Fe and Ru. These structures contain small, monodentate ligands from a set of ten ligands that span ligand field strengths and metal-coordinating atom identities (Figure 2). The initial set of 70 structures comprise all 10 possible homoleptic complexes. The remaining 60 heteroleptic complexes randomly sample a space of 180 complexes that can be formed with combinations of two ligands out of our set of ten ligands. We consider two geometries where the equatorial plane is both symmetric, i.e., comprises four identical ligands with a different axial ligand, and cissymmetric, i.e., comprises two unique ligands each of which is cis to each other, with an axial ligand that is the same as one of the two unique equatorial ligands (Figure 2 and Supporting Information Tables S3 and S4). The complexes with macrocyclic ligands were directly adapted from separate prior work⁷³ from which we only considered 543 Fe complexes from the initial set of catalysts for which the DFT geometry optimization of the Fe-oxo intermediate had successfully converged. The 543 Ru counterparts of these complexes were newly generated in the present work by a direct metal substitution. In these complexes, the equatorial positions are all occupied by a realistic tetradentate macrocyclic ligand constructed using known ligand fragments, and the axial position contains a monodentate ligand from the set of aniline, phenol, phenylphosphine, and thiophenol in both neutral and anionic forms that is coordinating to the metal via the 2p/3p

heteroatoms of the ligand from the pnictogen (N, P) and chalcogen (O, S) families (Figure 2 and Supporting Information Figure S2).⁷³ Thus, in this work, a theoretical set of 1506 Fe or Ru catalysts was considered prior to elimination of failed calculations (see Sec. 3).

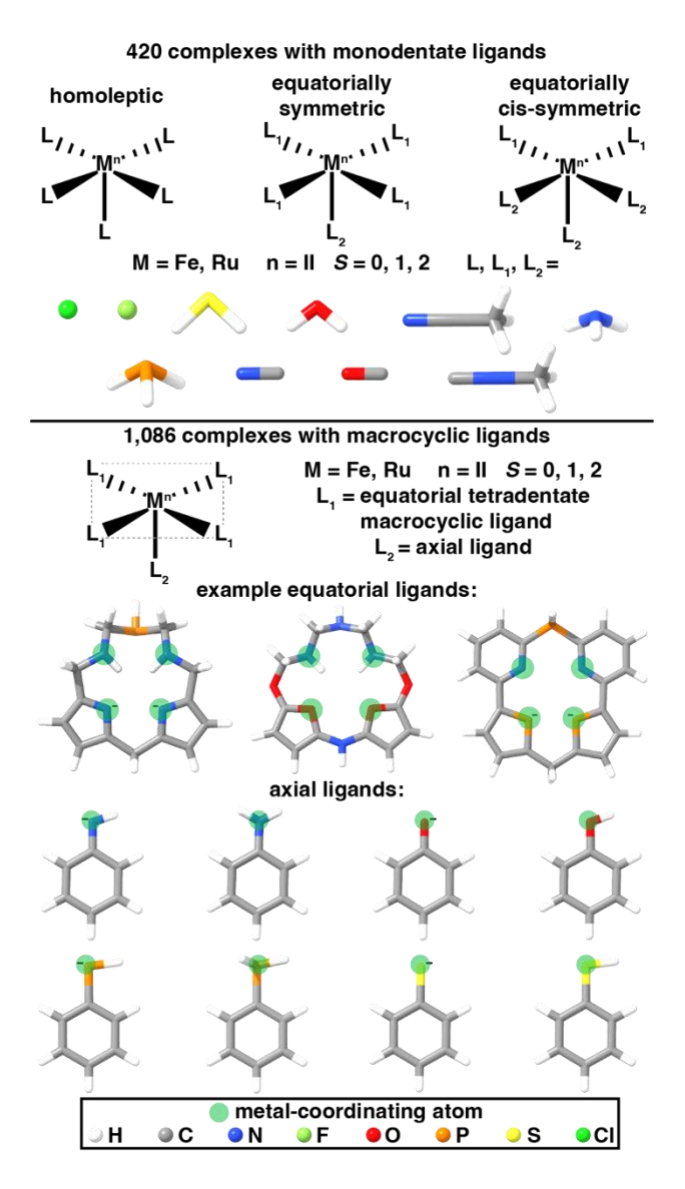


Figure 2. (top) Structural configurations of the 420 square pyramidal complexes (210 Fe and 210 Ru) with monodentate ligands. The set of ten small, monodentate ligands used to construct these complexes are shown ordered based on increasing ligand field strength and each complex comprises up to two unique ligands. Complexes in this set can be homoleptic with five identical monodentate ligands, equatorially symmetric where the equatorial ligands are identical with a different axial ligand or equatorially *cis*-symmetric where the equatorial plane consists of two unique ligands that are each *cis* to each other and the axial ligand is identical to one of the equatorial ligands. (bottom) Structural configuration of the 1,086 square pyramidal complexes (543 Fe and 543 Ru) with a tetradentate macrocyclic ligand in the equatorial plane and a monodentate axial

ligand. Three examples of tetradentate equatorial ligands and all eight axial ligands that are used to construct this set of complexes are shown with the metal-coordinating atom shaded in translucent green circles. Atom color codes: H in white, C in gray, N in blue, O in red, F in light green, P in orange, S in yellow, and Cl in green.

3. Computational Details.

All gas-phase geometry optimizations and single-point energy calculations were performed using density functional theory (DFT) with a development version of TeraChem v1.9. 98,99 The B3LYP¹⁰⁰⁻¹⁰² global hybrid functional with the empirical D3 dispersion correction¹⁰³ using Becke–Johnson damping¹⁰⁴ was employed for all calculations. The LACVP* composite basis set was used, which consists of a LANL2DZ effective core potential^{105,106} for Fe and Ru and the 6-31G* basis set¹⁰⁷ for all other atoms. Basis set sensitivity tests show that basis set superposition error is not a substantial factor contributing to trends in reaction energies (Supporting Information Figure S3). As in prior work, ^{72,91} we focus on relative energetics over a large data set, and thus we neglect solvent corrections and zero-point vibrational energy or entropic corrections to avoid a prohibitive increase in computational cost.

Singlet calculations were carried out in a spin-restricted formalism while calculations of all other spin states were performed in an unrestricted formalism. Level shifting 108 of 0.25 Ha was applied to both majority- and minority-spin virtual orbitals to aid self-consistent field (SCF) convergence to an unrestricted solution. Geometry optimizations were carried out with the translation rotation internal coordinate (TRIC) optimizer 109 using the BFGS algorithm with default convergence thresholds of maximum energy gradient of 4.5×10^{-4} hartree/bohr and energy difference between steps of 10^{-6} hartree.

The initial Fe and Ru mononuclear octahedral metal-oxo geometries were constructed using molSimplify¹¹⁰ with monodentate and macrocyclic ligand combinations adapted from prior work.^{73,97} From the optimized metal-oxo geometry, we functionalized the metal-oxo structure with a hydrogen atom to generate initial structures for the metal-hydroxo species and removed the oxo moiety to generate initial structures for the resting state, as done in prior work.⁷² Initial structures of the isopropanol-bound species were generated by adding an isopropyl group to the optimized metal-hydroxo structure (Supporting Information Figure S4). The workflow of DFT calculations begins by optimizing the metal-oxo geometries in three spin states: low spin (LS), intermediate spin (IS), and high spin (HS), and calculations of subsequent intermediates are only attempted following successful calculations of prior intermediates while conserving the spin state. Thus, we go from an S = 0 (LS), 1 (IS), 2 (HS) metal-oxo to an S = 0 (LS), 1 (IS), 2 (HS) resting state and from an S = 1/2 (LS), 3/2 (IS), 5/2 (HS) metal-hydroxo to S = 0 (LS), 1 (IS), 2 (HS) isopropanol-bound intermediate (Supporting Information Text S2).

Job submission was automated by molSimplify^{110,111} with a 24 h wall-time limit per run with up to five resubmissions. Geometry optimizations were carried out with geometry checks¹¹² prior to each resubmission and structures that failed any checks were eliminated (Supporting Information Table S5). Open-shell structures were also eliminated from the data set following established checks,^{71,112,113} if the expectation value of the \hat{S}^2 operator deviated from its expected value of S(S+1) by > 1 or the combined Mulliken spin density on the metal and the oxygen in the active site moiety differed from the total spin by > 1 μ B (Supporting Information Text S2 and Table S6).

To maximize correspondence, we only compare Fe and Ru complexes with identical ligands (i.e., they only differ by metal identity) that have successful DFT calculations for all

studied intermediates. This produces a final set of 222 Fe and Ru catalysts. Reaction energetics are compared across identical spin states (Supporting Information Table S6). For spin splitting energy comparisons, we restrict ourselves only to the spin splitting energy between the IS and LS states (i.e., $\Delta E_{\text{I-L}} = E(\text{IS}) - E(\text{LS})$) for a given intermediate because of the high failure rate of DFT calculations of Ru complexes in the HS state, particularly for the complexes with macrocyclic ligands (Supporting Information Table S7).

Multiwfn¹¹⁴ was used to calculate electronic properties of the metal-oxo intermediate such as the Mulliken spin density for the oxygen atom, the metal-oxo Mayer bond order,¹¹⁵ and the oxygen Mayer bond valence,¹¹⁵ which is the sum of the bond order between the oxygen atom and the transition metal. We selected the Mulliken population analysis due to its simplicity and low computational cost while Mayer bond order analysis was used because of its ability to describe bonding in systems with unpaired electrons.

Free energy landscapes of select Fe and Ru complexes were obtained using ORCA v5.0.1¹¹⁶ with the B3LYP functional with D3 dispersion correction using Becke–Johnson damping. The def2-TZVP basis set¹¹⁷ was employed for Fe and Ru atoms while the def2-SVP basis set¹¹⁷ was used for all other atoms. Starting from TeraChem-optimized structures, we completed additional DFT geometry optimizations to obtain thermochemical corrections on the intermediates. We used ORCA for the free energy landscape calculations because TeraChem does not support analytical Hessians. Transition states were optimized on ORCA by first computing potential energy surface (PES) scans where the presumed transition state mode, such as a bond length, was incrementally changed and fixed while geometry optimizing all other degrees of freedom. The maxima from these PES scans were used as initial guesses for a partitioned rational-function optimization (P-RFO)¹¹⁸ to locate the transition state structures. Transition state structures

were verified by performing frequency calculations to ensure that an imaginary frequency corresponding to the expected transition state mode was observed and intrinsic reaction coordinate (IRC)¹¹⁹ calculations to confirm the equilibrium points connecting a transition state structure. Minimum energy crossing points (MECPs) were obtained for two of the Ru complexes with macrocyclic ligands at their metal-oxo intermediates, metal-oxo formation transition states, and isopropanol-bound intermediates. The MECPs were calculated between a degenerate open-shell singlet and triplet structure and were located using the MECP implementation in ORCA v5.0.1¹²⁰ at the same level of theory as that used to compute the full free energy landscapes.

We benchmarked our DFT spin splitting energies on representative Fe and Ru complexes using CCSD(T). 121-125 Here, we employed DLPNO-CCSD(T) 126-129 with improved iterative (*T*₁) approximations 129 to the perturbative triple excitations as our reference method because the DLPNO local correlation approximation to CCSD(T) has demonstrated reliable accuracy in transition metal complexes. 130,131 DLPNO-CCSD(T) single-point energies for all non-singlet states were calculated with an unrestricted formalism and for singlet states with a restricted formalism. The single-point energies of all radical rebound intermediates of these complexes were extrapolated to the complete basis set limit by performing calculations with the def2-SVP and def2-TZVP basis sets on ORCA v5.0.1. The optimized geometries of the intermediates from B3LYP-D3 geometry optimizations using the def2-TZVP basis set for Fe and Ru atoms and the def2-SVP basis set for all other atoms were used as initial geometries and the corresponding Kohn-Sham orbitals were used as reference determinants for the DLPNO-CCSD(T) single-point calculations (Supporting Information Tables S8 and S9). 132

4. Results and Discussion.

4a. Effect of Spin State on Catalyst Reaction Energetics.

We first evaluate the influence of spin state on the energetics of propane to isopropanol conversion by Fe and Ru catalysts. We compare the $\Delta E(\text{oxo})$, $\Delta E(\text{HAT})$, and $\Delta E(\text{release})$ reaction energies of catalysts comprising identical ligands and spin states and that differ only by metal identity. In all three spin states, we find that the metal-oxo formation is generally favorable for both Fe and Ru catalysts (Figure 3 and Supporting Information Figures S5 and S6). Notably, Ru catalysts exhibit more favorable metal-oxo formation energies than Fe catalysts for all spin states. In the LS state, while the $\Delta E(\text{oxo})$ reaction energies for Fe and Ru catalysts are close (average values of -23 kcal/mol and -28 kcal/mol, respectively), oxo formation is slightly more favorable for Ru. However, in the IS and HS states, the favorability of metal-oxo formation in Ru catalysts over Fe catalysts becomes much more pronounced (on average by ca. 22 kcal/mol in the IS state and 31 kcal/mol in the HS state, Figure 3 and Supporting Information Figures S5 and S6). On average, we find that Fe catalysts have larger metal-oxo bond orders and shorter metal-oxo bond lengths compared to Ru catalysts, which would normally be indicative of greater stability of Feoxo species over Ru-oxo species (Supporting Information Figures S7 and S8). 72,74 Instead, our findings indicate that differences in metal chemistry are not well captured by these electronic descriptors, and the relative metal-oxo formation favorability is significantly influenced by the spin state of the metal.

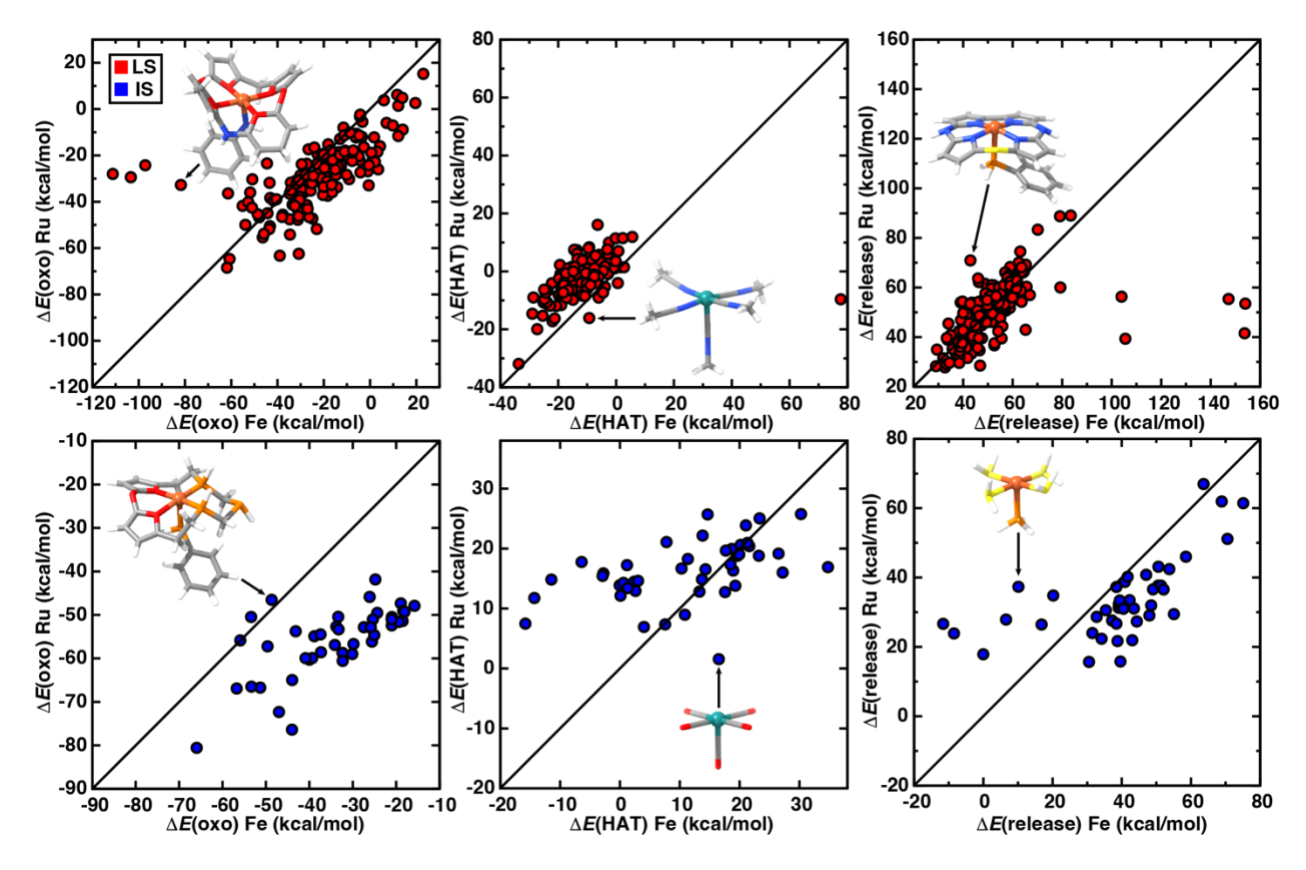


Figure 3. Parity plots of (left) $\Delta E(\text{oxo})$, (middle) $\Delta E(\text{HAT})$, and (right) $\Delta E(\text{release})$ for identical catalysts in the final data set with either Fe or Ru, all in kcal/mol. A similar set of plots with outliers truncated for clarity is provided in Supporting Information Figure S5. The red points (top) correspond to the LS state and the blue points (bottom) correspond to the IS state. The HS states are not shown due to the small number of successful HS calculations, but these results are shown in Supporting Information Figure S6. Insets depict representative complexes that deviate from the prevailing parity trends. Atom color codes for inset catalyst structures: Fe in brown, Ru in turquoise, C in gray, O in red, N in blue, S in yellow, P in orange, and H in white.

In all three spin states, we find that HAT is more favorable for Fe catalysts on average (by ca. 9 kcal/mol for LS, 5 kcal/mol for IS, and 9 kcal/mol for HS states) than for Ru catalysts (Figure 3 and Supporting Information Figures S5 and S6). Interestingly, Ru catalysts predominantly have positive $\Delta E(\text{HAT})$ values in higher-spin states (i.e., 2–26 kcal/mol in the IS state and 5–23 kcal/mol in HS states). Indeed, contrary to the trends observed in the $\Delta E(\text{oxo})$ values, the disparity in Fe and Ru $\Delta E(\text{HAT})$ values does not become more pronounced with higher-spin states but remains consistent (Figure 3 and Supporting Information Figures S5 and S6). We note that we select the

optimal radical-coupling convention for both metals during HAT (i.e., α -radical transfer for Fe catalysts and β -radical transfer for Ru catalysts) as informed by prior literature⁷² as well as the spin splitting energies of the metal-hydroxo species (see Sec. 4b), but we still observe more favorable $\Delta E(\text{HAT})$ values in Fe than Ru catalysts (Supporting Information Figure S9). Taken with the trends in $\Delta E(\text{oxo})$, this would suggest that selecting a catalyst spin state to target favorable $\Delta E(\text{oxo})$ in Fe or Ru will have a limited effect on $\Delta E(\text{HAT})$ values, suggesting weak trade-offs between these two steps, which we will explore in more detail next.

Examining the release energies (ΔE (release)), we find that both Fe and Ru catalysts exhibit high ΔE (release) values (i.e., > 20 kcal/mol for all spin states, with the exception of some Fe outliers in the IS and HS states), suggesting that isopropanol release could become rate-limiting regardless of metal identity (Figure 3 and Supporting Information Figures S5 and S6).^{73,74} These ΔE (release) values are higher in this work compared to prior work⁷³ because we selected catalysts from prior work with release energies that had not yet been optimized with evolutionary algorithms. Nevertheless, in the LS state, the Fe and Ru ΔE (release) values are quite comparable (52 kcal/mol and 50 kcal/mol on average, respectively, Figure 3 and Supporting Information Figures S5 and S6). In the IS and HS states, we generally find that ΔE (release) is more favorable in Ru catalysts over Fe catalysts by ca. 10 kcal/mol for both IS and HS states on average after removal of Fe outliers with ΔE (release) < 20 kcal/mol. We note that the Fe outliers in the higherspin states are exclusively catalysts with monodentate ligands that predominantly contain nitrogencoordinating ligands (Supporting Information Figures S10 and S11). The comparatively favorable ΔE (release) values of these outliers primarily arise from substantial destabilization of the isopropanol-bound intermediates coupled with either stabilization or only slight destabilization of the resting state in the higher-spin states, as judged from the spin splitting energies (see Sec. 4b). Focusing instead on the macrocyclic catalysts that do not exhibit notably low release energetics and comprise neutral and anionic analogs of axial ligands, we observe that the presence of anionic axial ligands slightly improves release energetics by reducing the overall charge on the catalyst, and thus the electrostatic attraction to bound isopropanol, as seen in prior work (Supporting Information Figure S12).⁷³

Given the prior focus^{72,75,78,79,91} on linear free energy relationships (LFERs) between $\Delta E(\text{oxo})$ and $\Delta E(\text{HAT})$, we explored whether Fe and Ru catalysts had distinct tradeoffs evident in metal-specific LFERs (Figure 4 and Supporting Information Figures S13 and S14). Averaged over all spin states, we find that Ru catalysts show a clearer correlation between $\Delta E(\text{oxo})$ and $\Delta E(\text{HAT})$ reaction energies (Pearson's R = -0.86) with a relatively steep slope (-0.52) while Fe catalysts show a weaker correlation (Pearson's R = -0.34) with a more gradual slope (-0.24, Figure 4 and Supporting Information Figure S13 and Table S10). Thus, Ru catalysts adhere more closely to the metal-oxo formation vs. HAT LFER observed in single-site heterogeneous catalysts, albeit with a steeper trade-off (literature slopes around -0.45 to -0.43) than those observed in prior work (Supporting Information Table S10). That is consistent with trends observed in homogeneous catalysis where metal-oxo vs. HAT LFERs are more readily disrupted. This presents a greater opportunity in optimizing Fe catalysts for C–H activation.

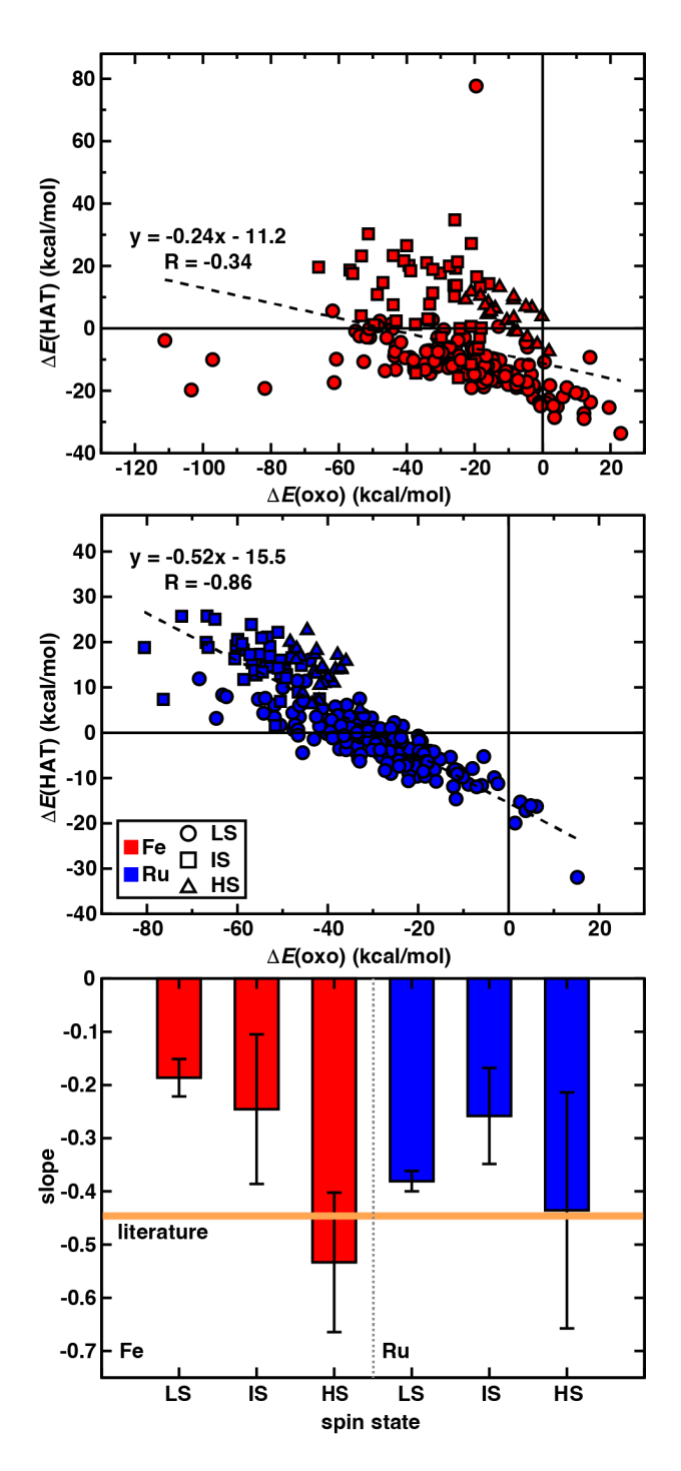


Figure 4. $\Delta E(\text{HAT})$ as a function of $\Delta E(\text{oxo})$ in kcal/mol for (top) Fe catalysts and (middle) Ru catalysts in the final set of 222 Fe and Ru complexes. A similar set of plots with outliers truncated for clarity is provided in Supporting Information Figure S13. In these plots, the points are distinguished by spin state (LS in circles, IS in squares, and HS in triangles). The best-fit lines across all data associated with each metal are shown as insets. (bottom) $\Delta E(\text{HAT})$ vs. $\Delta E(\text{oxo})$ LFER slopes and standard errors in 6 metal/spin state combinations. The range of literature slopes obtained for single-site and bulk heterogeneous catalysts is indicated by the shaded orange area. The data is colored by metal with Fe in red and Ru in blue.

For 3d transition metal homogeneous catalysts, the metal-oxo formation vs. HAT LFER is known to exhibit strong spin-state dependence. 72 Here, we also observe varying degrees of LFER correlation when the $\Delta E(\text{HAT})$ vs. $\Delta E(\text{oxo})$ data is categorized according to spin state. Considering the high count of LS data points in our dataset, it is unsurprising that in the LS state, these correlations closely align with the overall scaling relations for both metals (Figure 4 and Supporting Information Figure S13). In the HS state, however, we see that the strengths of the correlations are reversed wherein Fe catalysts exhibit a moderate correlation between $\Delta E(\text{oxo})$ and $\Delta E(\text{HAT})$ energies (Pearson's R = -0.66) while Ru catalysts exhibit a weak correlation (Pearson's R = -0.39) (Figure 4 and Supporting Information Figure S13). This can be attributed to greater difficulty in stabilizing and converging HS states in Ru compared to Fe, which likely introduced more variability in the HS state Ru data. In the IS state, we observe weak correlations for both Fe and Ru catalysts (Pearson's R = -0.26 and -0.40, respectively), with Ru catalysts still demonstrating a stronger correlation relative to Fe catalysts (Figure 4 and Supporting Information Figure S13). Beyond the large set of LS state data, it becomes evident that Ru catalysts in higher-spin states may also disrupt the metal-oxo formation vs. HAT scaling relation as in their Fe counterparts as well as other 3d homogeneous catalysts.

We also investigate the impact of ligand field strength on the metal-oxo formation vs. HAT reaction energetics as reported in prior literature. 72,86,91,92 We find that the spin state of the catalyst dictates how ligand field strength influences the reaction energetics. Consistent with prior work, 72 in higher-spin states (IS and HS states), we generally observe that catalysts comprising weak-field oxygen-containing ligands exhibit favorable HAT energies at the expense of less favorable metal-oxo formation energies (Supporting Information Figure S15). In the LS state, the trends are reversed wherein catalysts with strong-field carbene or substituted isocyanide ligands have

unfavorable $\Delta E(\text{oxo})$ values but very favorable $\Delta E(\text{HAT})$ energies (Supporting Information Figure S15). We note that the diversity and size of our dataset leads to broad distributions of the metal-oxo formation and HAT reaction energetics for sets of catalysts with ligands of qualitatively similar field strength. Nonetheless, these trends are more pronounced for Fe catalysts than Ru catalysts, particularly in higher-spin states, which suggests a greater degree of tunability via modulating the ligand field in C–H activation reactivity for Fe catalysts.

4b. Trends in Spin State Preferences.

The sensitivity of propane-to-isopropanol reaction energetics (i.e., especially of the metal-oxo formation energy) to the catalyst spin state motivates comparisons of the spin splitting energies where we have abundant data, i.e., in the IS and LS states (see Sec. 3). We carry out this comparison for Fe and Ru catalysts that share identical ligands and where both the IS and LS states converged to determine if there are differences in the spin–reactivity trends governing C–H hydroxylation by Fe and Ru catalysts through the radical rebound mechanism.

We begin by examining intermediates in the first half of the reaction coordinate: the resting state species and the metal-oxo intermediate. At the resting state, we find that Ru catalysts generally have positive $\Delta E_{\text{I-L}}$ (resting) values (ca. 13 kcal/mol on average) suggesting a strong preference for Ru catalysts to remain in the LS state regardless of the nature of the ligands present (Figure 5 and Supporting Information Figures S16 and S17). On the contrary, most Fe catalysts exhibit negative $\Delta E_{\text{I-L}}$ (resting) values (ca. -8 kcal/mol on average) suggesting that the IS state is better stabilized (Figure 5 and Supporting Information Figures S16 and S17). After excluding outliers, for Fe we generally observe that ligand field strength influences the ground state spin with weak-field ligands (oxygen- and sulfur-coordinating e.g., pyran, water, and thiopyran) favoring the IS state and strong-field ligands (carbon-coordinating e.g., methyl isocyanide and carbonyl)

favoring the LS state (Supporting Information Figure S17). Consistent with this trend, many Fe catalysts exhibit near-zero $\Delta E_{\rm LL}$ (resting) values (< |5 kcal/mol| for 38% of Fe catalysts), most of which comprise moderate-field nitrogen-coordinating ligands (e.g., acetonitrile and ammonia) (Figure 5 and Supporting Information Figures S16 and S17). This suggests facile interconversion between the LS and IS states at the resting state for Fe catalysts (Figure 5 and Supporting Information Figures S16 and S17). At the metal-oxo intermediate, the IS state is preferable over the LS state for both Fe and Ru catalysts by 28 kcal/mol for Fe and 22 kcal/mol for Ru on average (Figure 5 and Supporting Information Figure S16). The stabilization of the IS state metal-oxo relative to the LS metal-oxo in Fe catalysts is only slightly greater (i.e., by ca. 6 kcal/mol) than that in Ru catalysts. Thus, the high favorability of metal-oxo formation in Ru catalysts, particularly in the IS state, can be attributed to the destabilization of the IS resting state species coupled with the stabilization of the Ru IS metal-oxo species.

Next considering the metal-hydroxo intermediate, we find that the Ru-hydroxo species exclusively have positive ΔE_{I-L} (hydroxo) values, most of which have large magnitudes (ca. 36 kcal/mol on average, Figure 5 and Supporting Information Figure S16). While we observe a positive relationship between ligand field strength and Ru ΔE_{I-L} (hydroxo) values, the large positive values of ΔE_{I-L} (hydroxo) nevertheless suggest that the Ru-hydroxo intermediates favor a LS state irrespective of the coordinating ligands (Supporting Information Figure S17). Thus, the existence of an IS Ru-hydroxo species is highly unlikely, justifying our earlier choice to model HAT with Ru complexes via β -radical transfer. For the Fe-hydroxo species, we find that the distribution of ΔE_{I-L} (hydroxo) has a median of 0.5 kcal/mol (Figure 5 and Supporting Information Figure S16). Furthermore, we see that this distribution is similarly influenced by ligand field strength with negative ΔE_{I-L} (hydroxo) values associated with weak-field ligands, positive ΔE_{I-L} (hydroxo) values

corresponding to strong-field ligands and the distribution center primarily constituted by moderate-field ligands (Supporting Information Figure S17). Hence, the Fe catalysts could undergo either α - or β -radical transfer during HAT. Because most $\Delta E_{I-L}(hydroxo)$ values are negative or slightly positive, α -radical transfer during HAT remains more probable for Fe catalysts, as indicated in prior work.⁷²

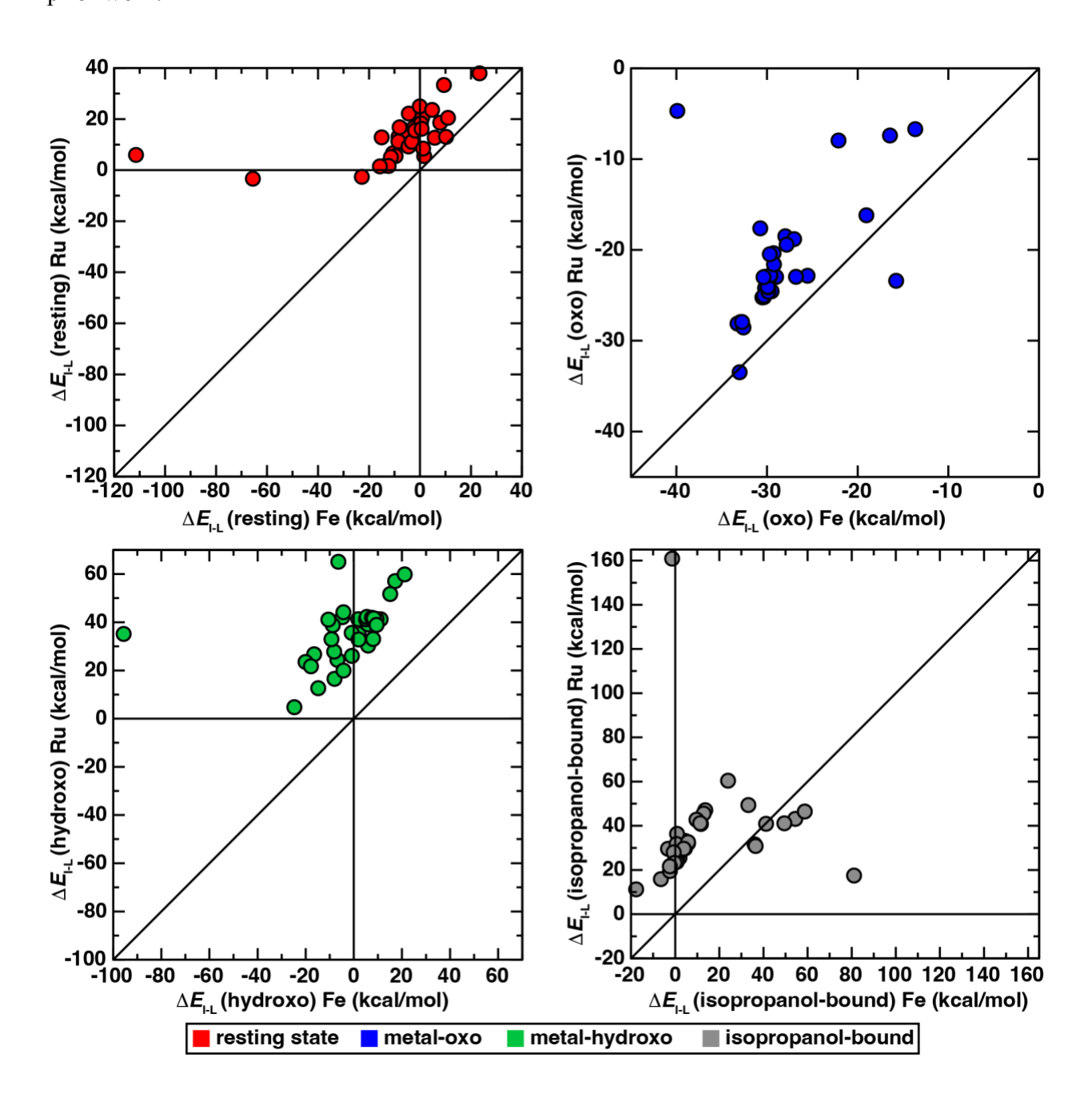


Figure 5. $\Delta E_{\text{I-L}} = E(\text{IS}) - E(\text{LS})$ parity plots for identical catalysts in the final data set with either Fe or Ru in kcal/mol for (top-left) the resting state, (top-right) the metal-oxo, (bottom-left) the metal-hydroxo, and (bottom-right) the isopropanol-bound intermediates. A similar set of plots with outliers truncated for clarity is provided in Supporting Information Figure S16. The data points are colored by radical rebound intermediate with resting state in red, metal-oxo in blue, metal-hydroxo in green, and isopropanol-bound in gray.

For the final isopropanol-bound intermediate, we again observe that the Ru catalysts have a strong preference towards the LS state irrespective of ligand field strength, with exclusively positive and large $\Delta E_{\text{I-L}}$ (isopropanol-bound) values averaging ca. 36 kcal/mol (Figure 5 and Supporting Information Figures S16 and S17). Consistent with prior work, ¹³³ Fe catalysts exhibit more variability in the preferred spin state at this intermediate, with most Fe catalysts having $\Delta E_{\text{I-}}$ L(isopropanol-bound) values close to zero (< |5 kcal/mol| for 50% of the Fe catalysts), indicating both IS and LS states can be accessible (Figure 5 and Supporting Information Figure S16). These Fe catalysts with small magnitudes of ΔE_{I-L} (isopropanol-bound) predominantly contain weak-field ligands while Fe catalysts with relatively larger ΔE_{I-L} (isopropanol-bound) values comprise moderate- and strong-field ligands (Supporting Information Figure S17). Thus, ligand field strength influences the ground state spin of the radical rebound intermediates in Fe catalysts. In specific outlier cases, some Fe catalysts comprising monodentate nitrogen-coordinating ligands have unexpectedly large, positive $\Delta E_{\text{I-L}}$ (isopropanol-bound) values, suggesting a strong preference for the LS state, which leads to highly favorable isopropanol release in the unstable IS state, as discussed earlier.

Taken together, the trends in spin splitting energies at each intermediate indicate that Ru catalysts could be expected to undergo a spin-forbidden pathway for radical rebound C–H hydroxylation, irrespective of the ligand environment in the catalyst because the ligand field strength plays a limited role in determining the ground state spin for Ru catalysts. Starting from

the resting state species in the LS state, the most favorable reaction energetics require that spin crossover occurs to form an IS Ru-oxo species followed by a β-radical transfer during HAT to form a LS Ru-hydroxo species with a ferromagnetically coupled •CH(CH₃)₂ radical that maintains the overall IS state. Subsequently, another spin crossover event should occur during the rebound of the isopropyl-radical to return to the preferred LS state at the isopropanol-bound intermediate. No further spin crossover events are needed, as release of the bound isopropanol should correspond to recovering a ground state LS Ru resting state structure.

From the distributions of ΔE_{I-L} values for the Fe catalysts, and considering that a majority of these catalysts favor the IS state in their resting state, we expect that Fe catalysts predominantly follow a spin-allowed pathway for C-H hydroxylation. Here, the IS resting state species is oxidized to form an IS Fe-oxo species that performs C–H activation in propane via an α-radical transfer to form an IS Fe-hydroxo species with an antiferromagnetically coupled •CH(CH₃)₂ radical, maintaining the overall triplet spin state following HAT. Thereafter, the isopropyl radical rebounds to form an IS isopropanol-bound intermediate and the IS resting state is recovered following isopropanol release. Nevertheless, for a small subset of catalysts for which we can converge all three spin (i.e., HS, IS, and LS) states, we find a greater degree of variability in preferred spin state of Fe catalysts than the equivalent Ru catalysts (Supporting Information Figure S18 and Text S3). While these conclusions may be expected to be somewhat sensitive to the functional chosen, ¹³³ qualitative trends are likely preserved. Depending on ligand chemistry, spinallowed pathways may be destabilized in favor of spin-forbidden pathways in Fe. In particular, strong-field ligands stabilize a LS resting state, Fe-hydroxo, and isopropanol-bound intermediates but not the Fe-oxo, which always remains in an IS ground state, whereas weak-field ligands all favor a spin-allowed IS catalytic cycle.

4c. Assessment of Relative Kinetic Trends in Fe and Ru Catalysts.

For six representative Fe and Ru complexes, we quantify differences in C–H hydroxylation kinetics by characterizing the full reaction coordinate (i.e., both transition states and reaction intermediates) with thermodynamic corrections for radical rebound propane hydroxylation. These six complexes, A–F, span nearly the full range of Ru ΔE_{I-L} (resting) values with three of them comprising macrocyclic ligands (A, D, and F) and the remaining three comprising monodentate ligands (B, C, and E) (Figure 6 and Supporting Information Figure S19). Complexes B, C, and E all comprise ammonia ligands on the equatorial plane with water, hydrogen sulfide, and fluoride axial ligands, respectively. The equatorial ligands of A, D, and F comprise macrocycles formed from two units each of two distinct fragments, with A containing dimethylphosphine and furan fragments, **D** containing thiopyran and dimethylthioether fragments, and **F** containing dimethylamine and dimethylether fragments. The axial ligands for complexes A, D, and F are phenylphosphanide, phenol, and anilide, respectively (Figure 6). We compute the full free energy landscapes in both the LS and IS states on the Fe and Ru analogues of these six complexes (Figure 7 and Supporting Information Figures S20–S23). For kinetic analysis, we employ 2,6dichloropyridine 1-oxide as the oxidant, which was used in previous experimental studies.³² In addition to its experimental relevance, we chose this oxidant because it is more rigid during Oatom donation compared to N₂O, which we have previously^{72,73,91} employed in computational studies, allowing for more straightforward convergence of transition states.

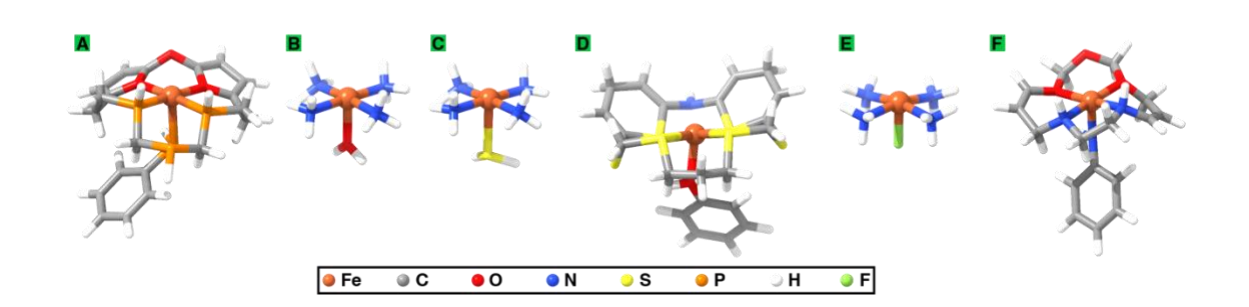


Figure 6. Fe analogues of complexes **A–F** selected for full free energy landscape calculations. Energy landscape calculations were also done on identical complexes with Ru centers (not shown here). Atom color codes: Fe in brown, C in gray, O in red, N in blue, S in yellow, P in orange, H in white, and F in light green.

In our free energy landscapes, the oxidant-bound intermediate serves as the reactant instead of the resting state species. We make this choice because we predict that the resting state would be extremely short-lived following isopropanol release because binding of the oxidant at the open metal site is very favorable (Supporting Information Figures S24–S28). We compute barriers for metal-oxo formation and HAT by starting with a relaxed potential energy surface scan, in which we constrain the N–O distance and O–H distance in metal-oxo formation and HAT, respectively, followed by a partitioned rational function optimization (P-RFO) on the highest-energy structure from the scan (see Sec. 3). For HAT, we ensure that we locate transition states associated with an α -radical transfer for Fe catalysts and β -radical transfer for Ru catalysts by inspecting the Mulliken spin densities (Supporting Information Text S4). We assume that the rebound of the isopropyl radical is barrierless and model isopropanol release as an unassisted dissociation 72-74,133 followed by rapid binding of 2,6-dichloropyridine 1-oxide, ignoring any kinetic barrier for this ligand exchange.

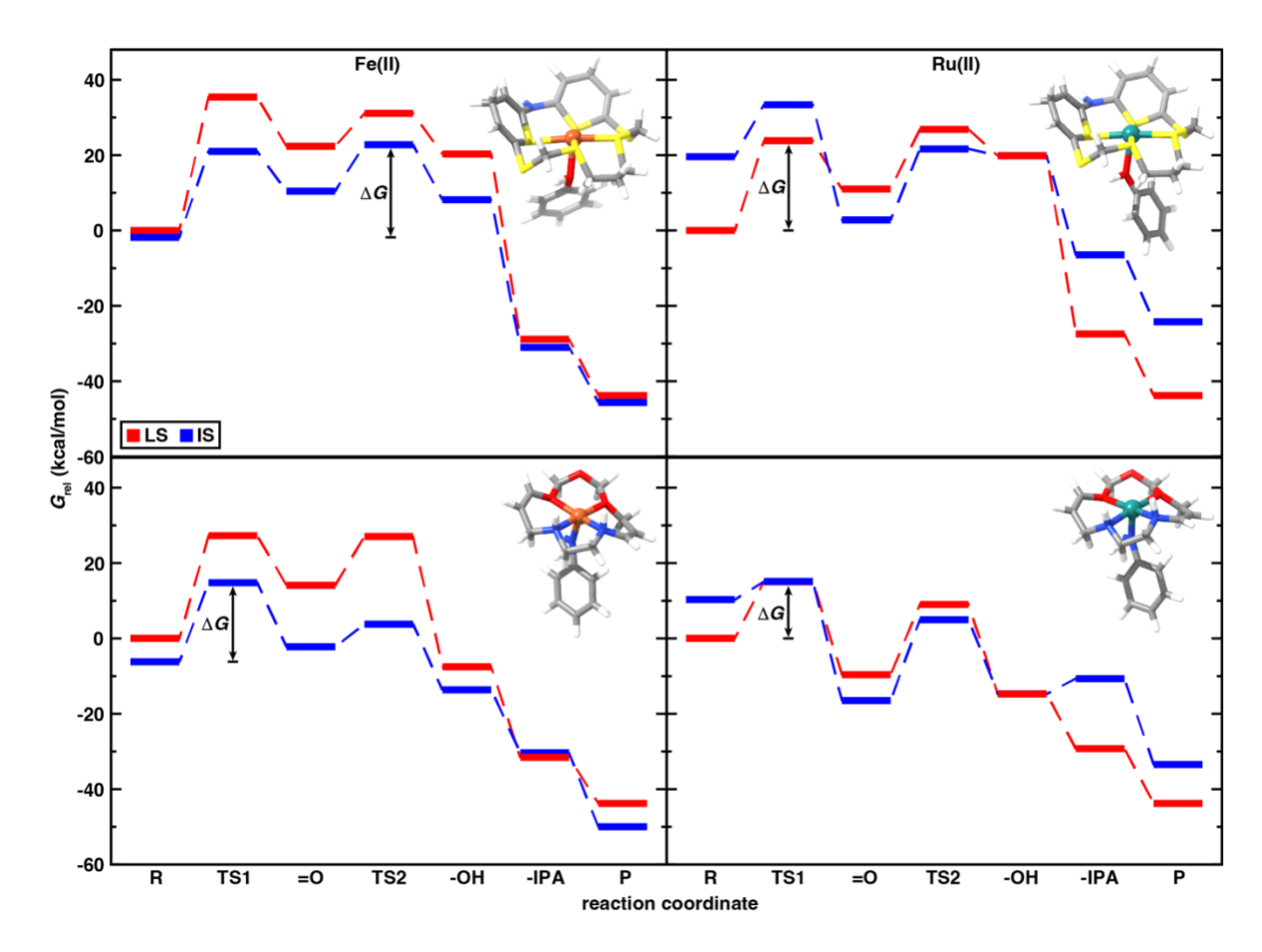


Figure 7. Gibbs free energy landscapes in kcal/mol of the (left) Fe and (right) Ru analogues of two representative complexes (**D**, top and **F**, bottom) on the LS state surface in red and the IS state surface in blue. All free energies are referenced with respect to the oxidant-bound intermediate (R) free energy in the LS state. The catalyst structures are shown as insets. The cycle proceeds from the reactants (R) to products (P) through the metal-oxo formation TS (TS1), the metal-oxo intermediate (=O), the HAT TS (TS2), the metal-hydroxo intermediate (-OH), and the isopropanol-bound intermediate (-IPA). The energetic spans, ΔG for each complex/metal combination assuming spin crossover is allowed are also shown as annotated insets. Of the four catalysts, only the energetic span of D with Ru depends on allowing spin-crossover. The alternative energetic span calculation without spin-crossover is provided in Supporting Information Table S12.

The free energy landscapes further substantiate the spin-reactivity trends we proposed from the spin splitting energy analyses. In our full catalytic cycle analysis, Fe catalysts predominantly undergo a spin-allowed C–H hydroxylation pathway on the IS state surface while Ru catalysts undergo a spin-forbidden pathway, transitioning between the LS and IS states (Figure 7 and Supporting Information Figures S20–S28). For a subset of complexes, **D** and **F**, selected for the

ease of convergence of those specific intermediates, we performed minimum energy crossing point (MECP) calculations on their Ru analogues (see Sec. 3). The MECP characterization confirms that the first spin crossover from the LS to the IS state during metal-oxo formation step occurs after the metal-oxo formation transition state (TS1) while the second spin crossover back to the LS state occurs during the radical rebound step (Supporting Information Table S11). We also find that the barriers for metal-oxo formation are lower in this subset of Ru catalysts (ca. 24 kcal/mol for **D** and 15 kcal/mol for **F** in LS states and 14 kcal/mol for **D** and 4 kcal/mol for **F** in IS states) than their corresponding Fe catalysts (ca. 35 kcal/mol for **D** and 27 kcal/mol for **F** in LS states and 23 kcal/mol for **D** and 21 kcal/mol for **F** in IS states). For HAT, we observe the opposite trend where the Fe catalysts generally have lower barriers (ca. 9 kcal/mol for **D** and 13 kcal/mol for **F** in LS states and 12 kcal/mol for **D** and 6 kcal/mol for **F** in IS states) than their Ru counterparts (ca. 16 kcal/mol for **D** and 19 kcal/mol for **F** in LS states and 19 kcal/mol for **D** and 21 kcal/mol for **F** in IS states) (Figure 7). This trend also holds more generally across all the six catalysts for which we computed reaction coordinates (Supporting Information Figures S20-S28). Furthermore, these kinetic trends align with the energetic trends for the metal-oxo formation and HAT steps, suggesting the existence of correlations between Fe and Ru C–H hydroxylation reaction energetics and kinetics, which we will return to in further detail.

To compare approximate catalytic turnover frequencies of Fe and Ru catalysts, we apply the energetic span model¹³⁴ to the Fe and Ru variants of catalysts **D** and **F** (Figure 7). For each catalyst/metal combination, we start from the ground state spin of the reactant species (R) and compute energetic spans for the cases where spin crossover is alternately allowed or disallowed (Supporting Information Table S12). In each of these cases, the turnover-determining intermediate (TDI) is the ground state spin of the oxidant-bound reactant species (R) because the exchange of

isopropanol with 2,6-dichloropyridine 1-oxide is exothermic for all catalyst/metal combinations. With the reactant serving as the TDI, the turnover-determining transition state (TDTS) is the one that maximizes the free energy difference relative to the TDI. When spin crossover is allowed, TS1 is the TDTS for Fe and Ru variants of complexes **D** and **F**, except for complex **D** with Fe where the HAT transition state (TS2) is the TDTS. When spin crossover is disallowed, both Fe and Ru variants for complex D have TS2 as the TDTS while complex F has TS1 as the TDTS (Figure 7 and Supporting Information Table S12).¹³⁴ As expected, Ru catalysts yield optimal energetic spans when spin crossover is allowed (ca. 24 kcal/mol for **D** and 15.1 kcal/mol for **F**) while for Fe catalysts, allowing or restricting spin crossover makes no difference on the resulting energetic spans (25 kcal/mol for **D** and 21 kcal/mol for **F**) since they proceed via spin-allowed C-H hydroxylation pathways (Figure 7 and Supporting Information Table S12). We note that one of the Fe catalysts has a LS ground state at the isopropanol-bound intermediate while the metalhydroxo intermediate and product have IS ground states (Figure 7). The IS isopropanol-bound intermediate, however, is only 1 kcal/mol higher in energy than the LS ground state, such that the reaction may proceed entirely on the IS state with no spin crossover to the LS state at this intermediate. Nevertheless, while the TDTS and TDI can be sensitive to the functional choice, 135 the energetic spans of the Fe and Ru catalysts are still qualitatively quite comparable. With Fe catalysts having similar energetic spans to the experimentally proven Ru catalysts while exhibiting spin-allowed pathways, we propose that Fe catalysts provide a comparatively better handle for tuning C-H activation reactivity over Ru catalysts. The experimental activity of Ru catalysts in the functionalization of C-H bonds in polyolefins is attributed to their compatibility with the reaction conditions including parameters like temperature, concentrations of reagents, and solvent

type.³² To harness the potential of Fe catalysts for this application, complementary screening measures can be employed that seek optimal reaction conditions by adjusting these parameters.

Expanding upon the observations from the free energy landscapes wherein trends in metaloxo formation and HAT activation energies behave similarly to the reaction energetic trends, we use our set of six catalysts to investigate the validity of the metal-oxo formation and HAT Brønsted-Evans-Polanyi (BEP) relations that are widely used to accelerate catalyst discovery. 73,78,83,89,91 Here, we consider the electronic barrier heights and energetics in the LS and IS states of the six Fe/Ru catalysts for which we characterize full reaction coordinates. For the metal-oxo formation step, in a given spin state, we define the activation energy, $E_a(oxo)$, and the metal-oxo formation energy, $\Delta E(\text{oxo})$, with respect to the oxidant-bound species (R) considered in the free energy landscapes. Despite the small dataset, the metal-oxo formation BEP appears to hold under our oxidant choice due to a strong correlation between $E_a(oxo)$ and $\Delta E(oxo)$ (Pearson's R = 0.96) with a slope of 0.45 (Figure 8 and Supporting Information Table S13). Furthermore, the quality of fit is independent of the spin state, the metal identity or ligand field (Figure 8). We note that among the six catalysts, the ammonia ligand is the most well-represented, yet the diversity in metal coordinating-atom identities is sufficient to establish a wide range of ligand field strengths (Supporting Information Figure S19). Prior studies that use N₂O as the oxidant show that the metaloxo formation BEP holds rather loosely and can widely vary as a function of metal-center out-ofplane distortions. 73,91 We attribute the BEP relationship holding more strongly to our choice of oxidant because, unlike N₂O that can distort through large-amplitude bending motions, 2,6dichloropyridine 1-oxide maintains its rigid structure during the N–O cleavage step. Because the oxidant used in this work does not undergo catalyst-dependent distortion, the relationship between energetics and barrier height is more likely to hold.⁷⁴

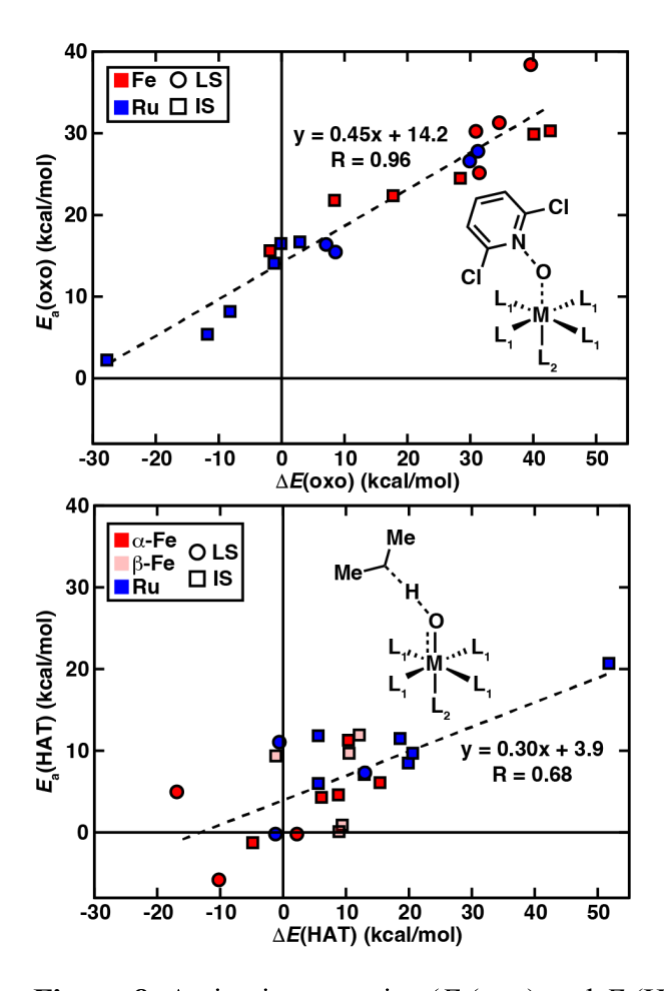


Figure 8. Activation energies (E_a (oxo) and E_a (HAT) in kcal/mol) vs. reaction energy, (ΔE (oxo) and ΔE (HAT) in kcal/mol) for the (top) metal-oxo formation and (bottom) HAT reaction steps. The data is colored by metal with Fe in red and Ru in blue. For the HAT reaction step, opaque red points correspond to an α-radical transfer while translucent red points correspond to a β-radical transfer in Fe complexes. The data points are also distinguished by spin state (LS in circles and IS in squares). The structure of the transition state along with a single best-fit line across all data associated with each reaction step are shown as insets.

Next, we examine the HAT BEP to see if as strong a relation holds as in the case of metaloxo formation. In each spin state, we define the activation energy, $E_a(HAT)$, and the HAT reaction energy, $\Delta E(HAT)$, with respect to the metal-oxo species. In our analysis, we consider HAT barriers and reaction energies for both the α - and β -radical transfers for the Fe catalysts in the IS state since Fe catalysts may proceed via either HAT pathway, with the α -radical transfer being more dominant as discussed earlier (Supporting Information Table S14). Contrary to the metal-oxo formation BEP, we find that the HAT BEP holds more loosely with a moderate correlation between $E_a(HAT)$ and $\Delta E(\text{HAT})$ (Pearson's R=0.68) (Figure 8 and Supporting Information Table S13). In some cases, we observe negative $E_a(\text{HAT})$ values because it is defined relative to infinitely separated reactants. Our HAT BEP slope of 0.30 also contrasts with the widely reported slope closer to $1.^{73,83,91}$ However, most prior studies showing strong HAT BEP relations focus only on the α -radical transfer for HAT. 73,91 In addition to a small dataset, which is more sensitive to noise, we believe that the inclusion of β -radical transfer pathways for the Fe catalysts also disrupts the BEP significantly, as demonstrated in previous studies. 79

Taken together, the moderate correlation between HAT kinetics and reaction energetics and the strong correlation between metal-oxo formation kinetics and reaction energetics suggest that evaluation of kinetics is less important for finding optimal Fe/Ru C-H activation catalysts in comparison to systems where BEPs hold less strongly. Indeed, trends in activation energies for the metal-oxo formation and HAT steps of complexes A-F align with the thermodynamic trends with Ru catalysts generally having more favorable metal-oxo formation barriers while Fe catalysts generally have more favorable HAT barriers (Supporting Information Figure S29). We also observe correlations between the barriers of the two steps for complexes A-F but, due to the limited dataset on reaction barriers, quantitative inferences on the relationship between the barriers should be approached with caution (Supporting Information Figure S29). Generalizing from our study, because Fe catalysts have more favorable HAT energetics than Ru catalysts, the discovery of Fe catalysts that outperform Ru catalysts in C–H activation would only involve identifying candidates with lower metal-oxo formation energies. This is more feasible with Fe catalysts because minimizing metal-oxo formation energies may not result in an energetic penalty for HAT due to weaker scaling relations in Fe. While finding better-performing Ru catalysts would only involve identifying candidates with lower HAT energies, this would prove challenging without

compromising the favorability in metal-oxo formation because Ru catalysts are more constrained by the scaling relations. Overall, our comparison of Fe and Ru catalysts over a wider chemical space reveals the overlooked potential of earth-abundant Fe catalysts in polyolefin functionalization with better tunability in C–H activation reactivity.

5. Conclusions.

We carried out high-throughput computational screening to compare 222 Fe and Ru catalysts for modification of polyolefins via C–H functionalization. Using propane as a model compound for the radical rebound hydroxylation to form isopropanol, we identified strong sensitivity to spin state in the relative behavior of Fe and Ru catalysts. Ru catalysts had greater favorability for metal-oxo formation and isopropanol release over Fe catalysts, a trend that was more significant for higher-spin states. In contrast, Fe catalysts exhibited more favorable HAT energetics than Ru catalysts, with this disparity remaining consistent across varying spin states. These spin-state dependent trends made it challenging to identify a single global LFER, and we instead observed strong sensitivity to how well an LFER held within a fixed spin state. Overall qualitative LFER trends by metal nevertheless suggested that Ru catalysts adhere more strongly to a classic metal-oxo formation vs. HAT LFER in comparison to Fe where the LFER can be readily disrupted.

The trends in spin splitting energies between the LS and IS states at each intermediate revealed that Ru catalysts exhibit a spin-forbidden pathway for the radical rebound C–H hydroxylation independent of the catalyst ligand field, crossing over between the LS and IS states. Fe catalysts predominantly underwent spin-allowed C–H hydroxylation pathways on the IS state surface, although changes in the ligand chemistry for Fe catalysts could more readily destabilize spin-allowed pathways in favor of spin-forbidden pathways. These proposed spin–reactivity trends

were corroborated in the full free energy landscapes that we computed for six representative Fe and Ru catalysts. The spin-allowed pathways in Fe catalysts with comparable energetic spans to their Ru analogues suggested that Fe catalysts provide a better opportunity for tuning C–H activation reactivity over Ru catalysts. Kinetic information obtained from the full free energy landscapes was used to validate the existence of a strong BEP relationship for the metal-oxo formation step and a relatively weaker BEP for the HAT step arising partially from the inclusion of β-radical transfer pathways for the Fe catalysts in the HAT BEP analysis. Nevertheless, the presence of moderate-to-strong BEP relations suggested that knowledge of reaction energetics is sufficient in finding optimal C–H activation catalysts. Fe catalysts that outperform Ru catalysts should minimize metal-oxo formation energies without sacrificing relatively favorable HAT energies for Fe catalysts. Our high-throughput study, thus, reveals that Fe catalysts demonstrate promise for polyolefin functionalization. The discovery of realizable Fe catalysts, however, may also require optimization of reaction conditions in addition to reaction energetics to harness their complete potential for polyolefin functionalization.

ASSOCIATED CONTENT

Supporting Information. Control calculations for identifying polyolefin probe molecule; details on control calculations for identifying polyolefin probe molecule; shifts in $\Delta E(\text{oxo})$ when using oxidants other than N₂O; oxidation and spin states of Fe and Ru in different intermediates; Fe and Ru catalyst structures in the initial equatorially symmetric set; Fe and Ru catalyst structures in the initial equatorially *cis*-symmetric set; approach for constructing tetradentate macrocyclic ligands; basis-set sensitivity of $\Delta E(\text{oxo})$, $\Delta E(\text{HAT})$, and $\Delta E(\text{release})$; details on functionalization of intermediates; details on DFT job statistics; metrics for geometry checks; DFT job statistics on Fe and Ru complexes; DFT job statistics on HS Fe and Ru complexes; T_1 diagnostics on the intermediates of representative complexes; DLPNO-CCSD(T) vs. DFT $\Delta E_{\text{I-L}}$ energies on representative complexes; Fe and Ru energetics parity plots at LS and IS with outliers; Fe and Ru energetics parity plots at HS; $\Delta E(\text{oxo})$ vs. metal-oxo Mayer bond order and O Mayer bond valence; metal-oxo bond length vs. O Mayer bond valence; Ru $\Delta E(\alpha\text{-HAT})$ vs. $\Delta E(\beta\text{-HAT})$ at IS and HS; Fe and Ru energetics parity plots at LS and IS grouped by ligand field; Fe and Ru energetics parity plots at HS grouped by ligand field; Fe and Ru energetics parity plots at HS grouped by ligand field; Fe and Ru energetics with neutral vs.

anionic axial ligands; $\Delta E(\text{HAT})$ vs. $\Delta E(\text{oxo})$ LFER for Fe and Ru with outliers; $\Delta E(\alpha\text{-HAT})$ vs. $\Delta E(\text{oxo})$ LFER for Fe and Ru; linear fits for $\Delta E(\text{HAT})$ vs. $\Delta E(\text{oxo})$ LFER; $\Delta E(\text{HAT})$ vs. $\Delta E(\text{oxo})$ LFER for Fe and Ru grouped by ligand field; Fe and Ru ΔE_{I-L} parity plots at each intermediate with outliers; Fe and Ru $\Delta E_{\text{I-L}}$ parity plots at each intermediate grouped by ligand field; favorable spin state distributions for Fe and Ru at each intermediate; details on favorable spin state distributions at each intermediate; selection of complexes for free energy landscape calculations; free energy landscape of complex A referenced to oxidant-bound species; free energy landscape of complex B referenced to oxidant-bound species; free energy landscape of complex C referenced to oxidant-bound species; free energy landscape of complex E referenced to oxidant-bound species; free energy landscapes of complexes **D** and **F** referenced to resting state; free energy landscape of complex A referenced to resting state; free energy landscape of complex B referenced to resting state; free energy landscape of complex C referenced to resting state; free energy landscape of complex E referenced to resting state; details on transition state searching; MECPs for complexes **D** and **F** with Ru; energetic span analysis of complexes **D** and **F**; outliers omitted from metal-oxo formation and HAT BEP plots; free energy changes and barriers for β-HAT in complexes **A-F** with Fe; $E_a(HAT)$ vs. $E_a(oxo)$ for complexes **A-F** (PDF)

Optimized structures of all reactive intermediates of the Fe and Ru catalysts in the final dataset; approximate transition state structures from the calculated reaction coordinates; raw electronic energies for all Fe and Ru catalysts in the final dataset; Fe and Ru catalysts that were discarded during DFT are available at Zenodo: 10.5281/zenodo.10207735

Data statement:

All data presented in the paper is available as supporting information in both a PDF summary as well as a ZIP file on Zenodo (10.5281/zenodo.10207735) containing structures and energetics of all catalysts studied.

AUTHOR INFORMATION

Corresponding Author

*email:hjkulik@mit.edu

CRediT author statement

Husain Adamji: conceptualization, writing - initial draft, writing - review & editing, investigation, formal analysis, data curation. Ilia Kevlishvili: supervision, conceptualization, writing - review & editing, investigation, formal analysis. Aditya Nandy: supervision, data curation. Yuriy Román-Leshkov: supervision, project administration, funding acquisition.

Heather J. Kulik: conceptualization, writing - review & editing, supervision, project administration, funding acquisition.

Declaration of interests

The authors declare no competing financial interest.

ACKNOWLEDGMENT

This work was primarily supported by the National Science Foundation under grant number CBET-1846426 (to H.A., I.K., A.N., and H.J.K.). This work was also supported by the U.S. Department of Energy, Office of Science, Office of Advanced Scientific Computing, Office of Basic Energy Sciences, via the Scientific Discovery through Advanced Computing (SciDAC) program (to H.A. and H.J.K.). The authors also thank the U.S. Department of Energy, Office of Basic Energy Sciences under Award DE-SC0016214 (for H.A. and Y.R.-L) for support. This work used Expanse at San Diego Supercomputing Center through allocation CHE140073 from the Advanced Cyberinfrastructure Coordination Ecosystem: Services and Support (ACCESS) program, which is supported by National Science Foundation Grants #2138259, #2138286, #2138307, #2137603, and #2138296. H.J.K. holds an Alfred P. Sloan Fellowship in Chemistry, which supported this work. The authors thank Adam H. Steeves for providing a critical reading of the manuscript.

REFERENCES

(1) Galli, P.; Vecellio, G. Polyolefins: The Most Promising Large-Volume Materials for the 21st Century. *J. Polym. Sci. A Polym. Chem.* **2004**, *42*, 396-415.

- (2) Boaen, N. K.; Hillmyer, M. A. Post-Polymerization Functionalization of Polyolefins. *Chem. Soc. Rev.* **2005**, *34*, 267-275.
- (3) Geyer, R.; Jambeck, J. R.; Law, K. L. Production, use, and fate of all plastics ever made. *Sci. Adv.* **2017**, *3*, e1700782.
- (4) Balzade, Z.; Sharif, F.; Ghaffarian Anbaran, S. R. Tailor-Made Functional Polyolefins of Complex Architectures: Recent Advances, Applications, and Prospects. *Macromolecules* **2022**, *55*, 6938-6972.
- (5) Domski, G. J.; Rose, J. M.; Coates, G. W.; Bolig, A. D.; Brookhart, M. Living Alkene Polymerization: New Methods for the Precision Synthesis of Polyolefins. *Prog. Polym. Sci.* **2007**, *32*, 30-92.
- (6) Coates, G. W.; Getzler, Y. D. Y. L. Chemical Recycling to Monomer for an Ideal, Circular Polymer Economy. *Nat. Rev. Mater.* **2020**, *5*, 501-516.
- (7) Rahimi, A.; García, J. M. Chemical Recycling of Waste Plastics for New Materials Production. *Nat. Rev. Chem.* **2017**, *1*, 0046.
- (8) Hamielec, A. E.; Gloor, P. E.; Zhu, S. Kinetics of, Free Radical Modification of Polyolefins in Extruders Chain Scission, Crosslinking and Grafting. *Can. J. Chem. Eng.* **1991**, *69*, 611-618.
- (9) Brewis, D. M.; Briggs, D. Adhesion to Polyethylene and Polypropylene. *Polymer* **1981**, 22, 7-16.
- (10) Chung, T. C. Synthesis of Functional Polyolefin Copolymers with Graft and Block Structures. *Prog. Polym. Sci.* **2002**, *27*, 39-85.
- (11) Williamson, J. B.; Lewis, S. E.; Johnson III, R. R.; Manning, I. M.; Leibfarth, F. A. C–H Functionalization of Commodity Polymers. *Angew. Chem. Int. Ed.* **2019**, *58*, 8654-8668.
- (12) Ittel, S. D.; Johnson, L. K.; Brookhart, M. Late-Metal Catalysts for Ethylene Homo- and Copolymerization. *Chem. Rev.* **2000**, *100*, 1169-1204.
- (13) Zhang, W.; Waddell, P. M.; Tiedemann, M. A.; Padilla, C. E.; Mei, J.; Chen, L.; Carrow, B. P. Electron-Rich Metal Cations Enable Synthesis of High Molecular Weight, Linear Functional Polyethylenes. *J. Am. Chem. Soc.* **2018**, *140*, 8841-8850.
- (14) Kenyon, P.; Wörner, M.; Mecking, S. Controlled Polymerization in Polar Solvents to Ultrahigh Molecular Weight Polyethylene. *J. Am. Chem. Soc.* **2018**, *140*, 6685-6689.
- (15) Boffa, L. S.; Novak, B. M. Copolymerization of Polar Monomers with Olefins Using Transition-Metal Complexes. *Chem. Rev.* **2000**, *100*, 1479-1494.
- (16) Nakamura, A.; Ito, S.; Nozaki, K. Coordination–Insertion Copolymerization of Fundamental Polar Monomers. *Chem. Rev.* **2009**, *109*, 5215-5244.
- (17) Franssen, N. M. G.; Reek, J. N. H.; de Bruin, B. Synthesis of Functional 'Polyolefins': State of the Art and Remaining Challenges. *Chem. Soc. Rev.* **2013**, *42*, 5809-5832.
- (18) Blasco, E.; Sims, M. B.; Goldmann, A. S.; Sumerlin, B. S.; Barner-Kowollik, C. 50th Anniversary Perspective: Polymer Functionalization. *Macromolecules* **2017**, *50*, 5215-5252.
- (19) Gauthier, M. A.; Gibson, M. I.; Klok, H.-A. Synthesis of Functional Polymers by Post-Polymerization Modification. *Angew. Chem. Int. Ed.* **2009**, *48*, 48-58.
- (20) Fazekas, T. J.; Alty, J. W.; Neidhart, E. K.; Miller, A. S.; Leibfarth, F. A.; Alexanian, E. J. Diversification of Aliphatic C–H Bonds in Small Molecules and Polyolefins Through Radical Chain Transfer. *Science* **2022**, *375*, 545-550.

- (21) Williamson, J. B.; Na, C. G.; Johnson, R. R., III; Daniel, W. F. M.; Alexanian, E. J.; Leibfarth, F. A. Chemo- and Regioselective Functionalization of Isotactic Polypropylene: A Mechanistic and Structure–Property Study. *J. Am. Chem. Soc.* **2019**, *141*, 12815-12823.
- (22) Shi, D.; Yang, J.; Yao, Z.; Wang, Y.; Huang, H.; Jing, W.; Yin, J.; Costa, G. Functionalization of Isotactic Polypropylene with Maleic Anhydride by Reactive Extrusion: Mechanism of Melt Grafting. *Polymer* **2001**, *42*, 5549-5557.
- (23) Moad, G. The Synthesis of Polyolefin Graft Copolymers by Reactive Extrusion. *Prog. Polym. Sci.* **1999**, *24*, 81-142.
- (24) Zhang, M.; Colby, R. H.; Milner, S. T.; Chung, T. C. M.; Huang, T.; deGroot, W. Synthesis and Characterization of Maleic Anhydride Grafted Polypropylene with a Well-Defined Molecular Structure. *Macromolecules* **2013**, *46*, 4313-4323.
- (25) Kondo, Y.; García-Cuadrado, D.; Hartwig, J. F.; Boaen, N. K.; Wagner, N. L.; Hillmyer, M. A. Rhodium-Catalyzed, Regiospecific Functionalization of Polyolefins in the Melt. *J. Am. Chem. Soc.* **2002**, *124*, 1164-1165.
- (26) Bae, C.; Hartwig, J. F.; Boaen Harris, N. K.; Long, R. O.; Anderson, K. S.; Hillmyer, M. A. Catalytic Hydroxylation of Polypropylenes. *J. Am. Chem. Soc.* **2005**, *127*, 767-776.
- (27) Bae, C.; Hartwig, J. F.; Chung, H.; Harris, N. K.; Switek, K. A.; Hillmyer, M. A. Regiospecific Side-Chain Functionalization of Linear Low-Density Polyethylene with Polar Groups. *Angew. Chem. Int. Ed.* **2005**, *44*, 6410-6413.
- (28) Díaz-Requejo, M. d. M.; Wehrmann, P.; Leathermann, M. D.; Trofimenko, S.; Mecking, S.; Brookhart, M.; Pérez, P. J. Controlled, Copper-Catalyzed Functionalization of Polyolefins. *Macromolecules* **2005**, *38*, 4966-4969.
- (29) Ray, A.; Zhu, K.; Kissin, Y. V.; Cherian, A. E.; Coates, G. W.; Goldman, A. S. Dehydrogenation of Aliphatic Polyolefins Catalyzed by Pincer-Ligated Iridium Complexes. *Chem. Commun.* **2005**, DOI:10.1039/B502120K 10.1039/B502120K, 3388-3390.
- (30) Boaen, N. K.; Hillmyer, M. A. Selective and Mild Oxyfunctionalization of Model Polyolefins. *Macromolecules* **2003**, *36*, 7027-7034.
- (31) Bunescu, A.; Lee, S.; Li, Q.; Hartwig, J. F. Catalytic Hydroxylation of Polyethylenes. *ACS Cent. Sci.* **2017**, *3*, 895-903.
- (32) Chen, L.; Malollari, K. G.; Uliana, A.; Sanchez, D.; Messersmith, P. B.; Hartwig, J. F. Selective, Catalytic Oxidations of C–H Bonds in Polyethylenes Produce Functional Materials with Enhanced Adhesion. *Chem* **2021**, *7*, 137-145.
- (33) Nesterov, D. S.; Nesterova, O. V. Catalytic Oxidations with *Meta*-Chloroperoxybenzoic Acid (m-CPBA) and Mono- and Polynuclear Complexes of Nickel: A Mechanistic Outlook. *Catalysts* **2021**, *11*, 1148.
- (34) Borovik, A. S. Role of Metal–Oxo Complexes in the Cleavage of C–H Bonds. *Chem. Soc. Rev.* **2011**, *40*, 1870-1874.
- (35) Price, J. C.; Barr, E. W.; Glass, T. E.; Krebs, C.; Bollinger, J. M. Evidence for Hydrogen Abstraction from C1 of Taurine by the High-Spin Fe(IV) Intermediate Detected During Oxygen Activation by Taurine: α-Ketoglutarate Dioxygenase (TauD). *J. Am. Chem. Soc.* **2003**, *125*, 13008-13009.
- (36) Price, J. C.; Barr, E. W.; Tirupati, B.; Bollinger, J. M.; Krebs, C. The First Direct Characterization of a High-Valent Iron Intermediate in the Reaction of an α-Ketoglutarate-Dependent Dioxygenase: A High-Spin Fe(IV) Complex in Taurine/α-Ketoglutarate Dioxygenase (TauD) from Escherichia coli. *Biochemistry* **2003**, *42*, 7497-7508.

- (37) Schulz, C. E.; Castillo, R. G.; Pantazis, D. A.; DeBeer, S.; Neese, F. Structure—Spectroscopy Correlations for Intermediate Q of Soluble Methane Monooxygenase: Insights from QM/MM Calculations. *J. Am. Chem. Soc.* **2021**, *143*, 6560-6577.
- (38) Engelmann, X.; Monte-Pérez, I.; Ray, K. Oxidation Reactions with Bioinspired Mononuclear Non-Heme Metal—Oxo Complexes. *Angew. Chem. Int. Ed.* **2016**, *55*, 7632-7649.
- (39) Nam, W. Synthetic Mononuclear Nonheme Iron–Oxygen Intermediates. *Acc. Chem. Res.* **2015**, *48*, 2415-2423.
- (40) Nam, W.; Lee, Y.-M.; Fukuzumi, S. Tuning Reactivity and Mechanism in Oxidation Reactions by Mononuclear Nonheme Iron(IV)-Oxo Complexes. *Acc. Chem. Res.* **2014**, *47*, 1146-1154.
- (41) Monte Pérez, I.; Engelmann, X.; Lee, Y.-M.; Yoo, M.; Kumaran, E.; Farquhar, E. R.; Bill, E.; England, J.; Nam, W.; Swart, M.; Ray, K. A Highly Reactive Oxoiron(IV) Complex Supported by a Bioinspired N₃O Macrocyclic Ligand. *Angew. Chem. Int. Ed.* **2017**, *56*, 14384-14388.
- (42) Yadav, V.; Rodriguez, R. J.; Siegler, M. A.; Goldberg, D. P. Determining the Inherent Selectivity for Carbon Radical Hydroxylation versus Halogenation with FeIII(OH)(X) Complexes: Relevance to the Rebound Step in Non-heme Iron Halogenases. *J. Am. Chem. Soc.* **2020**, *142*, 7259-7264.
- (43) Snyder, B. E. R.; Vanelderen, P.; Bols, M. L.; Hallaert, S. D.; Böttger, L. H.; Ungur, L.; Pierloot, K.; Schoonheydt, R. A.; Sels, B. F.; Solomon, E. I. The Active Site of Low-Temperature Methane Hydroxylation in Iron-Containing Zeolites. *Nature* **2016**, *536*, 317-321.
- (44) Snyder, B. E. R.; Böttger, L. H.; Bols, M. L.; Yan, J. J.; Rhoda, H. M.; Jacobs, A. B.; Hu, M. Y.; Zhao, J.; Alp, E. E.; Hedman, B.; Hodgson, K. O.; Schoonheydt, R. A.; Sels, B. F.; Solomon, E. I. Structural Characterization of a Non-Heme Iron Active Site in Zeolites That Hydroxylates Methane. *Proc. Natl. Acad. Sci.* **2018**, *115*, 4565-4570.
- (45) Snyder, B. E. R.; Bols, M. L.; Schoonheydt, R. A.; Sels, B. F.; Solomon, E. I. Iron and Copper Active Sites in Zeolites and Their Correlation to Metalloenzymes. *Chem. Rev.* **2018**, *118*, 2718-2768.
- (46) Xiao, D. J.; Bloch, E. D.; Mason, J. A.; Queen, W. L.; Hudson, M. R.; Planas, N.; Borycz, J.; Dzubak, A. L.; Verma, P.; Lee, K.; Bonino, F.; Crocellà, V.; Yano, J.; Bordiga, S.; Truhlar, D. G.; Gagliardi, L.; Brown, C. M.; Long, J. R. Oxidation of Ethane to Ethanol by N₂O in a Metal–Organic Framework with Coordinatively Unsaturated Iron(II) Sites. *Nat. Chem.* **2014**, *6*, 590-595.
- (47) Simons, M. C.; Vitillo, J. G.; Babucci, M.; Hoffman, A. S.; Boubnov, A.; Beauvais, M. L.; Chen, Z.; Cramer, C. J.; Chapman, K. W.; Bare, S. R.; Gates, B. C.; Lu, C. C.; Gagliardi, L.; Bhan, A. Structure, Dynamics, and Reactivity for Light Alkane Oxidation of Fe(II) Sites Situated in the Nodes of a Metal–Organic Framework. *J. Am. Chem. Soc.* **2019**, *141*, 18142-18151.
- (48) Osadchii, D. Y.; Olivos-Suarez, A. I.; Szécsényi, Á.; Li, G.; Nasalevich, M. A.; Dugulan, I. A.; Crespo, P. S.; Hensen, E. J. M.; Veber, S. L.; Fedin, M. V.; Sankar, G.; Pidko, E. A.; Gascon, J. Isolated Fe Sites in Metal Organic Frameworks Catalyze the Direct Conversion of Methane to Methanol. *ACS Catal.* **2018**, *8*, 5542-5548.

- (49) Rohde, J.-U.; In, J.-H.; Lim, M. H.; Brennessel, W. W.; Bukowski, M. R.; Stubna, A.; Münck, E.; Nam, W.; Que, L. Crystallographic and Spectroscopic Characterization of a Nonheme Fe(IV)=O Complex. *Science* **2003**, *299*, 1037-1039.
- (50) Klinker, E. J.; Kaizer, J.; Brennessel, W. W.; Woodrum, N. L.; Cramer, C. J.; Que Jr., L. Structures of Nonheme Oxoiron(IV) Complexes from X-ray Crystallography, NMR Spectroscopy, and DFT Calculations. *Angew. Chem. Int. Ed.* **2005**, *44*, 3690-3694.
- (51) Rohde, J.-U.; Torelli, S.; Shan, X.; Lim, M. H.; Klinker, E. J.; Kaizer, J.; Chen, K.; Nam, W.; Que, L. Structural Insights into Nonheme Alkylperoxoiron (III) and Oxoiron (IV) Intermediates by X-ray Absorption Spectroscopy. *J. Am. Chem. Soc.* **2004**, *126*, 16750-16761.
- (52) Ehudin, M. A.; Gee, L. B.; Sabuncu, S.; Braun, A.; Moënne-Loccoz, P.; Hedman, B.; Hodgson, K. O.; Solomon, E. I.; Karlin, K. D. Tuning the Geometric and Electronic Structure of Synthetic High-Valent Heme Iron(IV)-Oxo Models in the Presence of a Lewis Acid and Various Axial Ligands. *J. Am. Chem. Soc.* **2019**, *141*, 5942-5960.
- (53) Pestovsky, O.; Stoian, S.; Bominaar, E. L.; Shan, X.; Münck, E.; Que Jr., L.; Bakac, A. Aqueous Fe^{IV}=O: Spectroscopic Identification and Oxo-Group Exchange. *Angew. Chem. Int. Ed.* **2005**, *44*, 6871-6874.
- (54) Grapperhaus, C. A.; Mienert, B.; Bill, E.; Weyhermüller, T.; Wieghardt, K. Mononuclear (Nitrido)iron(V) and (Oxo)iron(IV) Complexes via Photolysis of [(cyclamacetato)Fe^{III}(N₃)]⁺ and Ozonolysis of [(cyclamacetato)Fe^{III}(O₃SCF₃)]⁺ in Water/Acetone Mixtures. *Inorg. Chem.* **2000**, *39*, 5306-5317.
- (55) Shaik, S.; Chen, H.; Janardanan, D. Exchange-Enhanced Reactivity in Bond Activation by Metal—Oxo Enzymes and Synthetic Reagents. *Nat. Chem.* **2011**, *3*, 19-27.
- (56) Janardanan, D.; Wang, Y.; Schyman, P.; Que Jr., L.; Shaik, S. The Fundamental Role of Exchange-Enhanced Reactivity in C-H Activation by S=2 Oxo Iron(IV) Complexes. *Angew. Chem. Int. Ed.* **2010**, *49*, 3342-3345.
- (57) Venturinelli Jannuzzi, S. A.; Phung, Q. M.; Domingo, A.; Formiga, A. L. B.; Pierloot, K. Spin State Energetics and Oxyl Character of Mn-Oxo Porphyrins by Multiconfigurational ab Initio Calculations: Implications on Reactivity. *Inorg. Chem.* **2016**, *55*, 5168-5179.
- (58) Rosen, A. S.; Notestein, J. M.; Snurr, R. Q. High-Valent Metal–Oxo Species at the Nodes of Metal–Triazolate Frameworks: The Effects of Ligand Exchange and Two-State Reactivity for C– H Bond Activation. *Angew. Chem.* **2020**, *132*, 19662-19670.
- (59) Geng, C.; Ye, S.; Neese, F. Analysis of Reaction Channels for Alkane Hydroxylation by Nonheme Iron(IV)—Oxo Complexes. *Angew. Chem. Int. Ed.* **2010**, *49*, 5717-5720.
- (60) Geng, C.; Ye, S.; Neese, F. Does a Higher Metal Oxidation State Necessarily Imply Higher Reactivity Toward H-Atom Transfer? A Computational Study of C–H Bond Oxidation by High-Valent Iron-Oxo and -Nitrido Complexes. *Dalton Trans.* **2014**, *43*, 6079-6086.
- (61) Ye, S.; Geng, C.-Y.; Shaik, S.; Neese, F. Electronic Structure Analysis of Multistate Reactivity in Transition Metal Catalyzed Reactions: the Case of C–H Bond Activation by Non-Heme Iron(iv)–Oxo Cores. *Phys. Chem. Chem. Phys.* **2013**, *15*, 8017-8030.
- (62) Kupper, C.; Mondal, B.; Serrano-Plana, J.; Klawitter, I.; Neese, F.; Costas, M.; Ye, S.; Meyer, F. Nonclassical Single-State Reactivity of an Oxo-Iron(IV) Complex Confined to Triplet Pathways. *J. Am. Chem. Soc.* **2017**, *139*, 8939-8949.
- (63) Groves, J. T.; Nemo, T. E. Aliphatic Hydroxylation Catalyzed by Iron Porphyrin Complexes. *J. Am. Chem. Soc.* **1983**, *105*, 6243-6248.

- (64) Chen, M. S.; White, M. C. Combined Effects on Selectivity in Fe-Catalyzed Methylene Oxidation. *Science* **2010**, *327*, 566-571.
- (65) Chen, L.; Su, X.-J.; Jurss, J. W. Selective Alkane C–H Bond Oxidation Catalyzed by a Non-Heme Iron Complex Featuring a Robust Tetradentate Ligand. *Organometallics* **2018**, *37*, 4535-4539.
- (66) Nandy, A.; Adamji, H.; Kastner, D. W.; Vennelakanti, V.; Nazemi, A.; Liu, M.; Kulik, H. J. Using Computational Chemistry To Reveal Nature's Blueprints for Single-Site Catalysis of C–H Activation. *ACS Catal.* **2022**, *12*, 9281-9306.
- (67) Oloo, W. N.; Que, L., Jr. Bioinspired Nonheme Iron Catalysts for C-H and C=C Bond Oxidation: Insights into the Nature of the Metal-Based Oxidants. *Acc. Chem. Res.* **2015**, 48, 2612-2621.
- (68) Wang, V. C. C.; Maji, S.; Chen, P. P. Y.; Lee, H. K.; Yu, S. S. F.; Chan, S. I. Alkane Oxidation: Methane Monooxygenases, Related Enzymes, and Their Biomimetics. *Chem. Rev.* **2017**, *117*, 8574-8621.
- (69) Costas, M.; Chen, K.; Que, L. Biomimetic Nonheme Iron Catalysts for Alkane Hydroxylation. *Coord. Chem. Rev.* **2000**, *200-202*, 517-544.
- (70) Shang, R.; Ilies, L.; Nakamura, E. Iron-Catalyzed C–H Bond Activation. *Chem. Rev.* **2017**, *117*, 9086-9139.
- (71) Nandy, A.; Zhu, J.; Janet, J. P.; Duan, C.; Getman, R. B.; Kulik, H. J. Machine Learning Accelerates the Discovery of Design Rules and Exceptions in Stable Metal–Oxo Intermediate Formation. *ACS Catal.* **2019**, *9*, 8243-8255.
- (72) Nandy, A.; Kulik, H. J. Why Conventional Design Rules for C–H Activation Fail for Open-Shell Transition-Metal Catalysts. *ACS Catal.* **2020**, *10*, 15033-15047.
- (73) Nandy, A.; Duan, C.; Goffinet, C.; Kulik, H. J. New Strategies for Direct Methane-to-Methanol Conversion from Active Learning Exploration of 16 Million Catalysts. *JACS Au* **2022**, *2*, 1200-1213.
- (74) Adamji, H.; Nandy, A.; Kevlishvili, I.; Román-Leshkov, Y.; Kulik, H. J. Computational Discovery of Stable Metal–Organic Frameworks for Methane-to-Methanol Catalysis. *J. Am. Chem. Soc.* **2023**, *145*, 14365-14378.
- (75) Rosen, A. S.; Notestein, J. M.; Snurr, R. Q. Structure-Activity Relationships That Identify Metal-Organic Framework Catalysts for Methane Activation. *ACS Catal.* **2019**, *9*, 3576-3587.
- (76) Rosen, A. S.; Notestein, J. M.; Snurr, R. Q. Identifying Promising Metal-Organic Frameworks for Heterogeneous Catalysis via High-Throughput Periodic Density Functional Theory. *J. Comput. Chem.* **2019**, *40*, 1305-1318.
- (77) Bligaard, T.; Nørskov, J. K.; Dahl, S.; Matthiesen, J.; Christensen, C. H.; Sehested, J. The Brønsted–Evans–Polanyi Relation and the Volcano Curve in Heterogeneous Catalysis. *J. Catal.* **2004**, *224*, 206-217.
- (78) Latimer, A. A.; Kulkarni, A. R.; Aljama, H.; Montoya, J. H.; Yoo, J. S.; Tsai, C.; Abild-Pedersen, F.; Studt, F.; Nørskov, J. K. Understanding Trends in C-H Bond Activation in Heterogeneous Catalysis. *Nat. Mater.* **2017**, *16*, 225-229.
- (79) Andrikopoulos, P. C.; Michel, C.; Chouzier, S.; Sautet, P. In Silico Screening of Iron-Oxo Catalysts for CH Bond Cleavage. *ACS Catal.* **2015**, *5*, 2490-2499.
- (80) Abild-Pedersen, F.; Greeley, J.; Studt, F.; Rossmeisl, J.; Munter, T. R.; Moses, P. G.; Skúlason, E.; Bligaard, T.; Nørskov, J. K. Scaling Properties of Adsorption Energies for

- Hydrogen-Containing Molecules on Transition-Metal Surfaces. *Phys. Rev. Lett.* **2007**, *99*, 016105.
- (81) Greeley, J. Theoretical Heterogeneous Catalysis: Scaling Relationships and Computational Catalyst Design. *Annu. Rev. Chem. Biomol. Eng.* **2016**, *7*, 605-635.
- (82) Wodrich, M. D.; Busch, M.; Corminboeuf, C. Accessing and Predicting the Kinetic Profiles of Homogeneous Catalysts from Volcano Plots. *Chem. Sci.* **2016,** *7*, 5723-5735.
- (83) Latimer, A. A.; Kakekhani, A.; Kulkarni, A. R.; Nørskov, J. K. Direct Methane to Methanol: The Selectivity–Conversion Limit and Design Strategies. *ACS Catal.* **2018**, *8*, 6894-6907.
- (84) Calle-Vallejo, F.; Loffreda, D.; Koper, M. T. M.; Sautet, P. Introducing Structural Sensitivity into Adsorption-Energy Scaling Relations by Means of Coordination Numbers. *Nat. Chem.* **2015,** *7*, 403-410.
- (85) Barona, M.; Ahn, S.; Morris, W.; Hoover, W.; Notestein, J. M.; Farha, O. K.; Snurr, R. Q. Computational Predictions and Experimental Validation of Alkane Oxidative Dehydrogenation by Fe₂M MOF Nodes. *ACS Catal.* **2020**, *10*, 1460-1469.
- (86) Liao, P.; Getman, R. B.; Snurr, R. Q. Optimizing Open Iron Sites in Metal-Organic Frameworks for Ethane Oxidation: A First-Principles Study. *ACS Appl. Mater. Interfaces* **2017**, *9*, 33484-33492.
- (87) Busch, M.; Wodrich, M. D.; Corminboeuf, C. Linear Scaling Relationships and Volcano Plots in Homogeneous Catalysis: Revisiting the Suzuki Reaction. *Chem. Sci.* **2015**, *6*, 6754-6761.
- (88) Cordova, M.; Wodrich, M. D.; Meyer, B.; Sawatlon, B.; Corminboeuf, C. Data-Driven Advancement of Homogeneous Nickel Catalyst Activity for Aryl Ether Cleavage. *ACS Catal.* **2020**, *10*, 7021-7031.
- (89) Schneider, J. E.; Goetz, M. K.; Anderson, J. S. Statistical Analysis of C-H Activation by Oxo Complexes Supports Diverse Thermodynamic Control over Reactivity. *Chem. Sci.* **2021**, *12*, 4173-4183.
- (90) Pellizzeri, S.; Barona, M.; Bernales, V.; Miró, P.; Liao, P.; Gagliardi, L.; Snurr, R. Q.; Getman, R. B. Catalytic Descriptors and Electronic Properties of Single-Site Catalysts for Ethene Dimerization to 1-Butene. *Catal. Today* **2018**, *312*, 149-157.
- (91) Gani, T. Z. H.; Kulik, H. J. Understanding and Breaking Scaling Relations in Single-Site Catalysis: Methane to Methanol Conversion by Fe^{IV}=O. *ACS Catal.* **2018**, *8*, 975-986.
- (92) Kirkland, J. K.; Khan, S. N.; Casale, B.; Miliordos, E.; Vogiatzis, K. D. Ligand Field Effects on the Ground and Excited States of Reactive FeO²⁺ species. *Phys. Chem. Chem. Phys.* **2018**, *20*, 28786-28795.
- (93) Khorshidi, A.; Violet, J.; Hashemi, J.; Peterson, A. A. How Strain Can Break the Scaling Relations of Catalysis. *Nat. Catal.* **2018**, *1*, 263-268.
- (94) Vitillo, J. G.; Lu, C. C.; Cramer, C. J.; Bhan, A.; Gagliardi, L. Influence of First and Second Coordination Environment on Structural Fe(II) Sites in MIL-101 for C–H Bond Activation in Methane. *ACS Catal.* **2021**, *11*, 579-589.
- (95) Szécsényi, Á.; Khramenkova, E.; Chernyshov, I. Y.; Li, G.; Gascon, J.; Pidko, E. A. Breaking Linear Scaling Relationships with Secondary Interactions in Confined Space: A Case Study of Methane Oxidation by Fe/ZSM-5 Zeolite. *ACS Catal.* **2019**, *9*, 9276-9284.
- (96) Groves, J. T.; McClusky, G. A. Aliphatic Hydroxylation via Oxygen Rebound. Oxygen Transfer Catalyzed by Iron. *J. Am. Chem. Soc.* **1976,** *98*, 859-861.

- (97) Nandy, A.; Chu, D. B. K.; Harper, D. R.; Duan, C.; Arunachalam, N.; Cytter, Y.; Kulik, H. J. Large-Scale Comparison of 3d and 4d Transition Metal Complexes Illuminates the Reduced Effect of Exchange on Second-Row Spin-State Energetics. *Phys. Chem. Chem. Phys.* **2020**, *22*, 19326-19341.
- (98) Seritan, S.; Bannwarth, C.; Fales, B. S.; Hohenstein, E. G.; Isborn, C. M.; Kokkila-Schumacher, S. I. L.; Li, X.; Liu, F.; Luehr, N.; Snyder Jr., J. W.; Song, C.; Titov, A. V.; Ufimtsev, I. S.; Wang, L.-P.; Martínez, T. J. TeraChem: A Graphical Processing Unit-Accelerated Electronic Structure Package for Large-Scale Ab Initio Molecular Dynamics. *WIREs Comput. Mol. Sci.* **2021**, *11*, e1494.
- (99) Petachem. TeraChem. http://www.petachem.com. (Accessed July 12, 2023).
- (100) Becke, A. D. Density-Functional Thermochemistry. III. The Role of Exact Exchange. *J. Chem. Phys.* **1993**, *98*, 5648-5652.
- (101) Lee, C.; Yang, W.; Parr, R. G. Development of the Colle-Salvetti Correlation-Energy Formula into a Functional of the Electron Density. *Phys. Rev. B* **1988**, *37*, 785-789.
- (102) Stephens, P. J.; Devlin, F. J.; Chabalowski, C. F.; Frisch, M. J. Ab Initio Calculation of Vibrational Absorption and Circular Dichroism Spectra Using Density Functional Force Fields. *J. Phys. Chem.* **1994**, *98*, 11623-11627.
- (103) Grimme, S.; Antony, J.; Ehrlich, S.; Krieg, H. A Consistent and Accurate Ab Initio Parametrization of Density Functional Dispersion Correction (DFT-D) for the 94 Elements H-Pu. *J. Chem. Phys.* **2010**, *132*, 154104.
- (104) Becke, A. D.; Johnson, E. R. A Density-Functional Model of the Dispersion Interaction. *J. Chem. Phys.* **2005**, *123*, 154101.
- (105) Wadt, W. R.; Hay, P. J. Ab Initio Effective Core Potentials for Molecular Calculations. Potentials for Main Group Elements Na to Bi. *J. Chem. Phys.* **1985**, *82*, 284-298.
- (106) Hay, P. J.; Wadt, W. R. Ab Initio Effective Core Potentials for Molecular Calculations: Potentials for the Transition Metal Atoms Sc to Hg. *J. Chem. Phys.* **1985**, *82*, 270-283.
- (107) Rassolov, V. A.; Pople, J. A.; Ratner, M. A.; Windus, T. L. 6-31G* Basis Set for Atoms K Through Zn. *J. Chem. Phys.* **1998**, *109*, 1223-1229.
- (108) Saunders, V. R.; Hillier, I. H. A "Level–Shifting" Method for Converging Closed Shell Hartree–Fock Wave Functions. *Int. J. Quantum Chem.* **1973**, *7*, 699-705.
- (109) Wang, L.-P.; Song, C. Geometry Optimization Made Simple with Translation and Rotation Coordinates. *J. Chem. Phys.* **2016**, *144*, 214108.
- (110) Ioannidis, E. I.; Gani, T. Z.; Kulik, H. J. molSimplify: A Toolkit for Automating Discovery in Inorganic Chemistry. *J. Comput. Chem.* **2016**, *37*, 2106-2117.
- (111) Group, K. molSimplify & molSimplify Automatic Design. https://github.com/hjkgrp/molsimplify. (Accessed July 25, 2022).
- (112) Duan, C.; Janet, J. P.; Liu, F.; Nandy, A.; Kulik, H. J. Learning from Failure: Predicting Electronic Structure Calculation Outcomes with Machine Learning Models. *J. Chem. Theory Comput.* **2019**, *15*, 2331-2345.
- (113) Nandy, A.; Duan, C.; Janet, J. P.; Gugler, S.; Kulik, H. J. Strategies and Software for Machine Learning Accelerated Discovery in Transition Metal Chemistry. *Ind. Eng. Chem. Res.* **2018**, *57*, 13973-13986.
- (114) Lu, T.; Chen, F. Multiwfn: A Multifunctional Wavefunction Analyzer. *J. Comput. Chem.* **2012**, *33*, 580-592.
- (115) Mayer, I. Bond Order and Valence Indices: A Personal Account. *J. Comput. Chem.* **2007**, 28, 204-221.

- (116) Neese, F. Software Update: The ORCA Program System—Version 5.0. WIREs Comput. Mol. Sci. 2022, 12, e1606.
- (117) Weigend, F.; Ahlrichs, R. Balanced Basis Sets of Split Valence, Triple Zeta Valence and Quadruple Zeta Valence Quality for H to Rn: Design and Assessment of Accuracy. *Phys. Chem. Chem. Phys.* **2005**, *7*, 3297-3305.
- (118) Baker, J. An Algorithm for the Location of Transition States. *J. Comput. Chem.* **1986,** 7, 385-395.
- (119) Cerjan, C. J.; Miller, W. H. On Finding Transition States. *J. Chem. Phys.* **1981,** 75, 2800-2806.
- (120) Harvey, J. N.; Aschi, M.; Schwarz, H.; Koch, W. The Singlet and Triplet States of Phenyl Cation. A Hybrid Approach for Locating Minimum Energy Crossing Points Between Non-Interacting Potential Energy Surfaces. *Theor. Chem. Acc.* **1998**, *99*, 95-99.
- (121) Mata, R. A.; Suhm, M. A. Benchmarking Quantum Chemical Methods: Are We Heading in the Right Direction? *Angew. Chem. Int. Ed.* **2017**, *56*, 11011-11018.
- (122) Mardirossian, N.; Head-Gordon, M. Thirty Years of Density Functional Theory in Computational Chemistry: An Overview and Extensive Assessment of 200 Density Functionals. *Mol. Phys.* **2017**, *115*, 2315-2372.
- (123) Bartlett, R. J.; Musiał, M. Coupled-Cluster Theory in Quantum Chemistry. *Rev. Mod. Phys.* **2007,** *79*, 291-352.
- (124) Knowles, P. J.; Hampel, C.; Werner, H. J. Coupled Cluster Theory for High Spin, Open Shell Reference Wave Functions. *J. Chem. Phys.* **1993**, *99*, 5219-5227.
- (125) Watts, J. D.; Gauss, J.; Bartlett, R. J. Coupled-Cluster Methods with Noniterative Triple Excitations for Restricted Open-Shell Hartree–Fock and Other General Single Determinant Reference Functions. Energies and Analytical Gradients. *J. Chem. Phys.* **1993**, *98*, 8718-8733.
- (126) Riplinger, C.; Neese, F. An Efficient and Near Linear Scaling Pair Natural Orbital Based Local Coupled Cluster Method. *J. Chem. Phys.* **2013**, *138*.
- (127) Riplinger, C.; Sandhoefer, B.; Hansen, A.; Neese, F. Natural Triple Excitations in Local Coupled Cluster Calculations with Pair Natural Orbitals. *J. Chem. Phys.* **2013**, *139*.
- (128) Guo, Y.; Riplinger, C.; Becker, U.; Liakos, D. G.; Minenkov, Y.; Cavallo, L.; Neese, F. Communication: An Improved Linear Scaling Perturbative Triples Correction for the Domain Based Local Pair-Natural Orbital Based Singles and Doubles Coupled Cluster Method [DLPNO-CCSD(T)]. *J. Chem. Phys.* **2018**, *148*.
- (129) Guo, Y.; Riplinger, C.; Liakos, D. G.; Becker, U.; Saitow, M.; Neese, F. Linear Scaling Perturbative Triples Correction Approximations for Open-Shell Domain-Based Local Pair Natural Orbital Coupled Cluster Singles and Doubles Theory [DLPNO-CCSD(T/T)]. *J. Chem. Phys.* **2020**, *152*.
- (130) Flöser, B. M.; Guo, Y.; Riplinger, C.; Tuczek, F.; Neese, F. Detailed Pair Natural Orbital-Based Coupled Cluster Studies of Spin Crossover Energetics. *J. Chem. Theory Comput.* **2020**, *16*, 2224-2235.
- (131) Drosou, M.; Mitsopoulou, C. A.; Pantazis, D. A. Reconciling Local Coupled Cluster with Multireference Approaches for Transition Metal Spin-State Energetics. *J. Chem. Theory Comput.* **2022**, *18*, 3538-3548.
- (132) Feldt, M.; Phung, Q. M.; Pierloot, K.; Mata, R. A.; Harvey, J. N. Limits of Coupled-Cluster Calculations for Non-Heme Iron Complexes. *J. Chem. Theory Comput.* **2019**, *15*, 922-937.

- (133) Vennelakanti, V.; Nandy, A.; Kulik, H. J. The Effect of Hartree-Fock Exchange on Scaling Relations and Reaction Energetics for C–H Activation Catalysts. *Top. Catal.* **2022**, *65*, 296-311.
- (134) Kozuch, S.; Shaik, S. How to Conceptualize Catalytic Cycles? The Energetic Span Model. *Acc. Chem. Res.* **2011**, *44*, 101-110.
- (135) Gani, T. Z.; Kulik, H. J. Unifying Exchange Sensitivity in Transition-Metal Spin-State Ordering and Catalysis through Bond Valence Metrics. *J. Chem. Theory Comput.* **2017**, *13*, 5443-5457.